Title

Impact of burned areas on the northern African seasonal climate from the perspective of regional modeling

Journal

Climate Dynamics, 47(11)

ISSN

0930-7575

Authors

De Sales, Fernando
Xue, Yongkang
Okin, Gregory S

Publication Date

2016-12-01

DOI

10.1007/s00382-015-2522-4

Peer reviewed

Clim Dyn
DOI 10.1007/s00382-015-2522-4

Impact of burned areas on the northern African seasonal climate from the perspective of regional modeling

Fernando De Sales · Yongkang Xue · Gregory S. Okin

Received: 18 September 2014 / Accepted: 13 February 2015

Abstract This study investigates the impact of burned areas on the surface energy balance and monthly precipitation in northern Africa as simulated by a state-of-the-art regional model. Mean burned area fraction derived from MODIS date of burning product was implemented in a set of 1-year long WRF-NMM/SSiB2 model simulations. Vegetation cover fraction and LAI were degraded daily based on mean burned area fraction and on the survival rate for each vegetation land cover type. Additionally, ground darkening associated with wildfire-induced ash and charcoal deposition was imposed through lower ground albedo for a period after burning. In general, wildfire-induced vegetation and ground condition deterioration increased mean surface albedo by exposing the brighter bare ground, which in turn caused a decrease in monthly surface net radiation. On average, the wildfire-season albedo increase was approximately 6.3 % over the Sahel. The associated decrease in surface available energy caused a drop in surface sensible heat flux to the atmosphere during the dry months of winter and early spring, which gradually transitioned to a more substantial decrease in surface evapotranspiration in April and May that lessened throughout the rainy season. Overall, post-fire land condition deterioration resulted in a decrease in precipitation over sub-Saharan Africa, associated with the weakening of the West African monsoon progression through the region. A decrease in atmospheric moisture flux convergence was observed in the burned area simulations, which played a dominant role in reducing precipitation in the area, especially in the months preceding the monsoon onset. The areas with the largest precipitation impact were those covered by savannas and rainforests, where annual precipitation decreased by 3.8 and 3.3 %, respectively. The resulting precipitation decrease and vegetation deterioration caused a drop in gross primary productivity in the region, which was strongest in late winter and early spring. This study suggests the cooling and drying of atmosphere induced by burned areas caused the strengthening of subsidence during pre-onset and weakening of upward atmospheric motion during onset and mature stages of the monsoon leading to a waning of convective instability and precipitation. Monthly mid-tropospheric vertical wind showed a strengthening of downward motion in winter and spring seasons, and weakening of upward movement during the rainy months. Furthermore, precipitation energy analysis revealed that most of precipitation decrease originated from convective events, which supports the hypothesis of reduced convective instability due to wildfires.

Keywords Impact of burned areas on regional climate · Regional climate modeling · Wildfire · Sahel precipitation · Sahel land cover change

This paper is a contribution to the special issue on West African climate decadal variability and its modeling, consisting of papers from the West African Monsoon Modeling and Evaluation (WAMME) and the African Multidisciplinary Monsoon Analyses (AMMA) projects, and coordinated by Yongkang Xue, Serge Janicot, and William Lau.

F. De Sales (✉) · Y. Xue · G. S. Okin
Department of Geography, University of California Los Angeles, Los Angeles, CA, USA
e-mail: fsales@ucla.edu

Y. Xue
Department of Atmospheric and Oceanic Sciences, University of California Los Angeles, Los Angeles, CA, USA

1 Introduction

The occurrence of wildfires, whether natural or human-made, is an important disturbance of the terrestrial

Published online: 25 February 2015

ecosystems (Bond et al. 2005) and it plays an essential role in shaping global and regional vegetation (Glenn-Lewin and van der Maarel 1992; Thonicke et al. 2001). Wildfires directly influences climate by destroying vegetation biomass, altering soil characteristics and surface albedo. Wildfires are also important sources of aerosol, CO_2, and trace gases to the atmosphere (Scholes et al. 1996; van der Werf et al. 2010).

A wildfire leaves behind scars in the landscape commonly known as burned areas. These areas are characterized by deposits of charcoal and ash from consumed plant biomass, removal of vegetation, and alteration of the vegetation structure and biomass distribution. Every year, during the dry season, large portions of Africa are affected by natural and anthropogenic wildfires which result in extensive burned areas. These burned areas are still poorly represented in climate models, and their effects on the climate have not been extensively investigated.

Surface albedo is crucial to land/atmosphere interactions so changes in surface reflectance associated with these burned areas should have a relevant role in these interactions. The Sahel region is located between the Sahara desert to the north and moist tropical Africa to the south. It is, thus, a transition zone between dry and moist climates and experiences significant precipitation variability on seasonal to inter-annual time scales.

Several studies have indicated a possible link between droughts in the Sahel and change in albedo (Courel et al. 1984; Xue et al. 1990; Xue 1997; Zheng and Eltahir 1997; Zeng et al. 1999). The main hypothesis is that a reduction in vegetation caused by drought, overgrazing, and deforestation for cropping triggers an increase in albedo, which in turn tends to weaken convective activity and to reinforce subsidence in the Sahel reducing precipitation. Sea surface temperature has been shown to be a major controller in the Sahel's inter-annual and seasonal precipitation variability, with feedbacks due to changes in surface albedo acting more as an amplifier of ocean driven variability than an initial trigger of monsoon variability (Giannini et al. 2003). Nonetheless, the role of land/atmosphere interaction on the Sahel climate has been confirmed by several climate modeling studies (e.g., Xue 1997; Clark et al. 2001; Li et al. 2007; Xue et al. 2010a; Ma et al. 2013).

The impact of burned areas on the surface albedo has been investigated by several observational, remote-sensing and modeling studies (e.g., Govaerts et al. 2002; Jin and Roy 2005; Myhre et al. 2005; Samain et al. 2008; Lyons et al. 2008; Bowman et al. 2009). Most of these studies have indicated that wildfires and resulting burned areas tend to decrease surface albedo at short time scales due to the deposition and ash and charcoal (Govaerts et al. 2002; Myhre et al. 2005). However, other investigations have indicated that burned areas tend to increase surface albedo over longer time periods owing to removal of land cover and consequent exposure of bare ground following wildfires (Lyons et al. 2008; Bowman et al. 2009).

Through a combined analysis of 5-year in situ radiation data and remotely sensed albedo, Samain et al. (2008) showed that wildfires caused a marked decreased of surface albedo of about 10 days in the Sahel. They determined that the reduction of ground reflectance is mainly due to accumulation of charred material that is quickly dispersed by wind. Moreover, they concluded that the removal of vegetation by wildfires can lead to an increase in albedo after dispersion of char by increasing the exposure of the (often brighter) bare ground. Other studies have shown that charcoal and ash deposition may last longer than 10 days (e.g., Govaerts et al. 2002). Jin and Roy (2005) utilized Moderate Resolution Imaging Spectroradiometer (MODIS) data to study wildfire-induced ground darkening in northern Australia. They estimated it to last between 16 to 32 days after a wildfire. Type and state of vegetation are probably relevant variables in determining wildfire-induced ground darkening intensity and duration.

The development of a comprehensive approach to implement the impact of wildfires on surface albedo in regional climate simulations has been scarce. Such an approach would allow a broader understanding of the impact of burned areas on surface hydrology, albedo, atmospheric circulation, and precipitation, which is difficult to accomplish via remote sensing and observation studies alone. Moreover, studies have demonstrated that regional climate models provide a reliable tool to study atmospheric circulations and land/atmosphere interactions at spatial scales beyond current general circulation model capabilities (De Sales and Xue 2011, 2013; Xue et al. 2014).

The present study aims to assess the effects of burned areas over northern Africa on surface climate and seasonal precipitation through a series of 1-year long regional climate model simulations. To accomplish this, the WRF-NMM regional climate model was implemented with the second version of the SSiB vegetation biophysical processes model (Xue et al. 1991; Zhan et al. 2003) and then run over a domain which encompasses the entire African continent.

A brief description of the regional model and a detailed explanation of the experimental design are presented in the next section. In Sect. 3, we present a detailed examination of simulation results including regional climate model evaluation and the impact of burned areas on northern Africa's albedo, radiation balance, and precipitation. A possible explanation for the effects of burned areas on precipitation and their implications on photosynthetic assimilation are provided in Sect. 4. As a final point, our conclusion remarks are presented in Sect. 5.

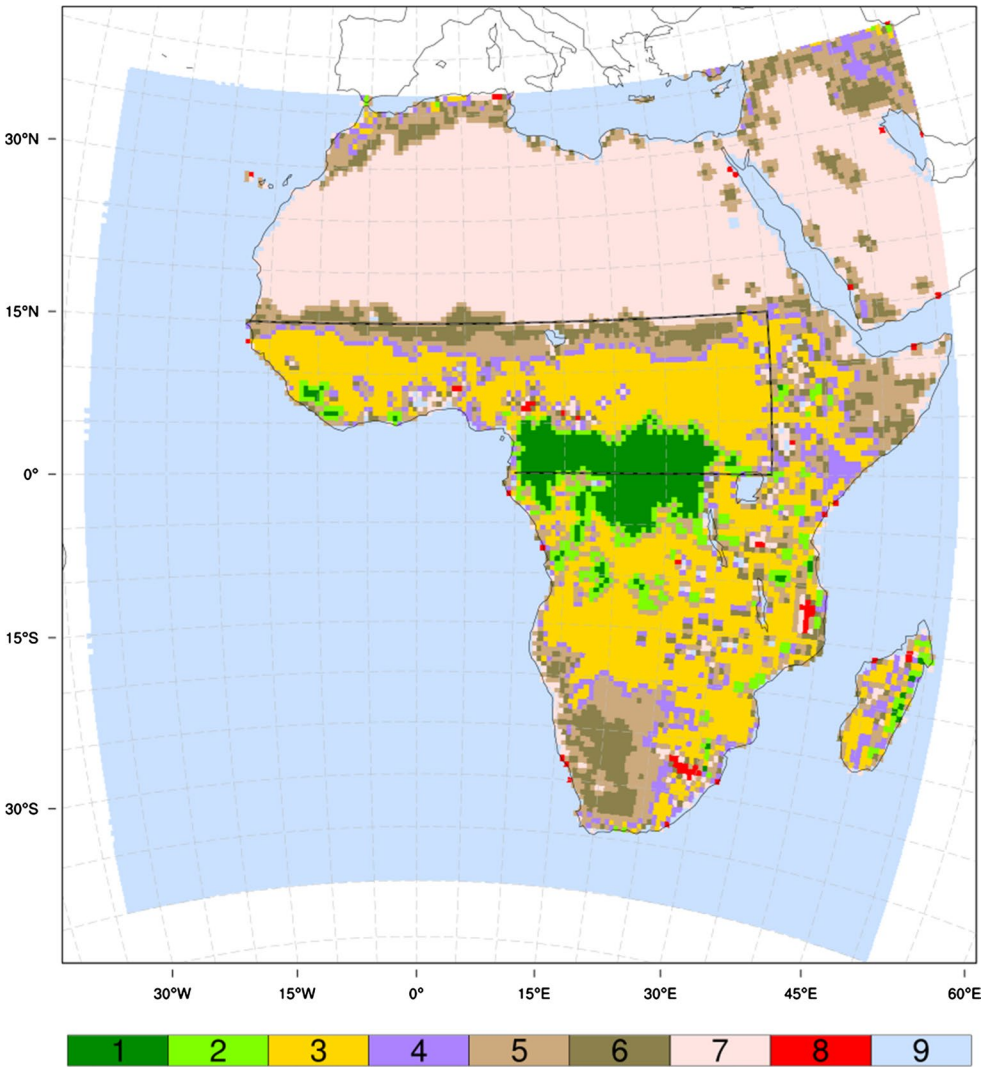

Fig. 1 The domain used for the WRF-NMM/SSiB2 simulations and its land cover type distribution. Land cover types are (*1*) rainforest, (*2*) other forests, (*3*) savanna, (*4*) grassland, (*5*) shrubs on grass, (*6*) shrubs on bare soil, (*7*) bare soil, (*8*) cropland, and (*9*) water. Area A is enclosed by the *solid lines* between 0° and 15°N and from the Atlantic coast to 35°E

2 The model, burned area data and experimental design

2.1 The model

The experiments in this study were carried out using the Nonhydrostatic Mesoscale Model core of the Weather Research and Forecasting (WRF-NMM) atmospheric regional model system (Janjic 2003; Janjic et al. 2001). The WRF-NMM is an advanced fully-compressible regional model currently maintained and supported by NOAA/NCEP and the Developmental Test-bed Center. For this study, the second version of the Simplified Simple Biosphere (SSiB-2) land surface model was implemented into the WRF-NMM. The SSiB-2 is a state-of-the-art vegetation biophysical model that estimates photosynthesis-controlled land surface processes, while preserving energy, water and momentum conservation at the atmosphere-land surface interface (Zhan et al. 2003). Hereafter, the atmosphere-land surface coupled model will be referred as WRF-NMM/SSiB2.

WRF-NMM/SSiB2 also includes the Betts-Miller-Janjic convective scheme (Janjic 1994), NOAA GFDL shortwave and longwave radiation schemes (Lacis and Hansen 1974; Schwarzkopf and Fels 1991), and Ferrier microphysics scheme (Ferrier 1994). The model was set up on a $0.5° \times 0.5°$ horizontal resolution with 38 vertical levels grid covering all of Africa and the adjoining oceans (Fig. 1). Distribution of land cover types in the model domain is also shown in Fig. 1.

2.2 Burned area data

The MODIS approximate date of burning product (MCD45) available at the University of Maryland, College Park, website (http://modis-fire.umd.edu), was used as the initial source of burned area information for this study. The dataset provides 500-m resolution maps of the approximate days of burning, which are obtained by locating the

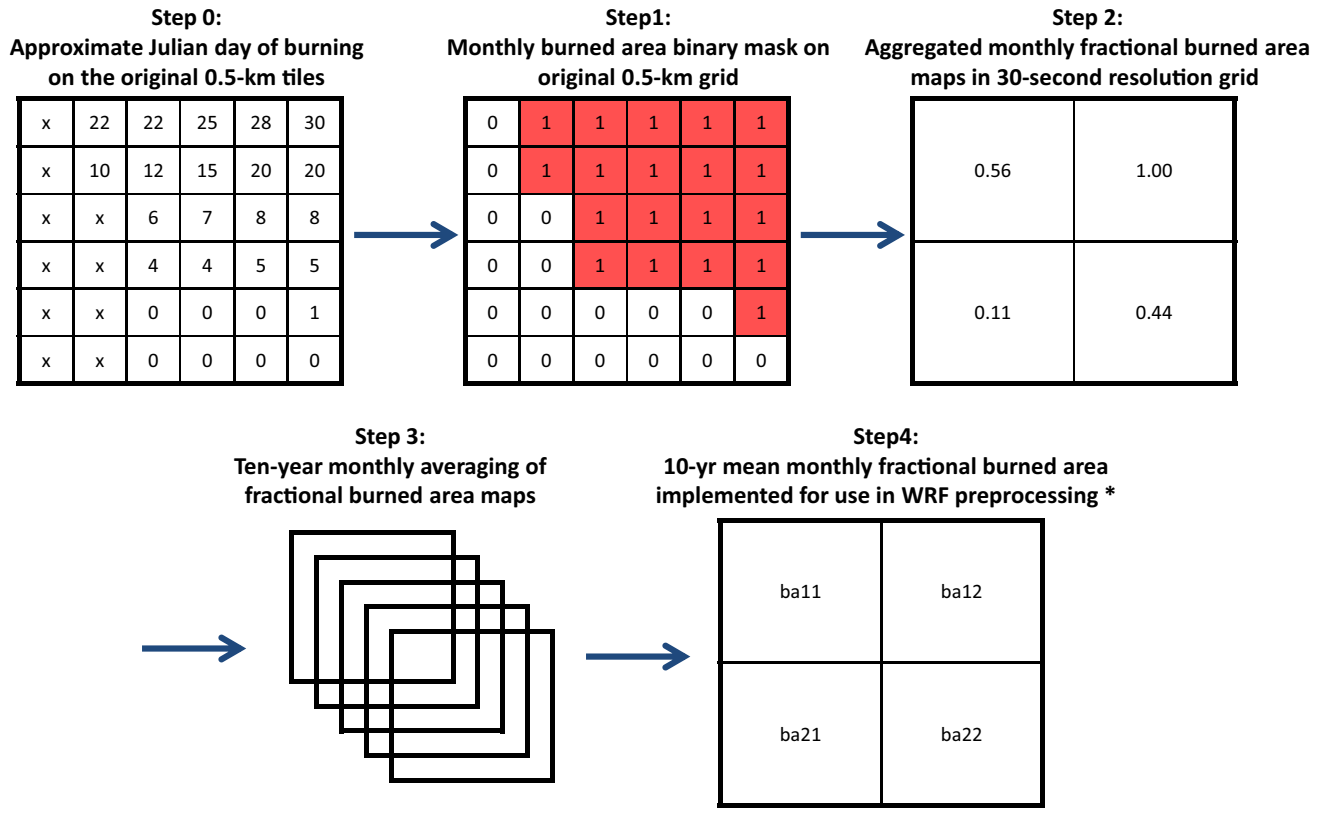

Fig. 2 Schematic diagram showing the methodology used to obtain the 10-year mean monthly fractional burned area from MODIS approximate date of burning products. Note: the numbers in the figures are for example purpose only. The *X symbol* in step 0 represents water, snow, or undefined values pixels, which were set to unburned on the burned area binary masks. (*) WRF preprocessing includes resampling of data onto model's grid and daily fractional burned area interpolation

occurrence of rapid changes in daily surface reflectance time series data as described by Roy et al. (2002, 2008).

MCD45 tiles from 2002 to 2011 were mosaicked to cover the entire WRF-NMM/SSiB2 domain (Fig. 1). Unburned-burned binary masks were then produced based on the Julian day of burning for each month of the dataset. Water and snow pixels, as well as those registered as undefined, were set to unburned (Fig. 2, steps 0 and 1).

The high-resolution monthly unburned-burned binary masks were then aggregated into 30-s resolution fractional burned area maps using a grid-cell averaging method (Fig. 2, step 2). From these data, 10-year monthly average fractional burned area maps were calculated and then implemented in the WRF-NMM/SSiB2 model (Fig. 2, steps 3 and 4). Two additional steps are not included in Fig. 2, namely the resampling of monthly average fractional burned area maps into the model's rotated Arakawa staggered E-grid and the linear interpolation of monthly fractional burned into daily values. These additional steps take place during the model integration runtime.

This time-averaging approach (Fig. 2, step 3) was chosen to minimize the effects of missing information resultant from those periods when the MODIS date-of-burning retrieval algorithm could not find enough data to determine ground reflectance, as well as the periods of sensor malfunctions and cloud contamination. Figure 3 shows the 10-year average annual burned area fraction map obtained by the process abovementioned. Burned areas are evident throughout the continent, except in the Sahara and southern Kalahari Deserts and the West African tropical rainforest. The most impacted regions are located in the Sahel and in south central Africa. Large expanses of burnt area fraction in excess of 0.5 can be seen in these regions, especially in between 20°E–35°E and 5°N–15°N in eastern and western sub-Saharan Africa, and 15°–25°E and 5°–15°S just south of the West Africa rainforest.

By combining the information on Figs. 1 and 3, the average impact of fire on the main vegetation types in the area A (Fig. 1 inset), which includes most of sub-Sahara's burned areas, can be estimated. Savanna is the most abundant vegetation type in the region covering approximately 43.6 % of the land (Table 1), followed by shrublands (23.6 %), rainforest (13.3 %), grassland (6.3 %), other forests (5.7 %),

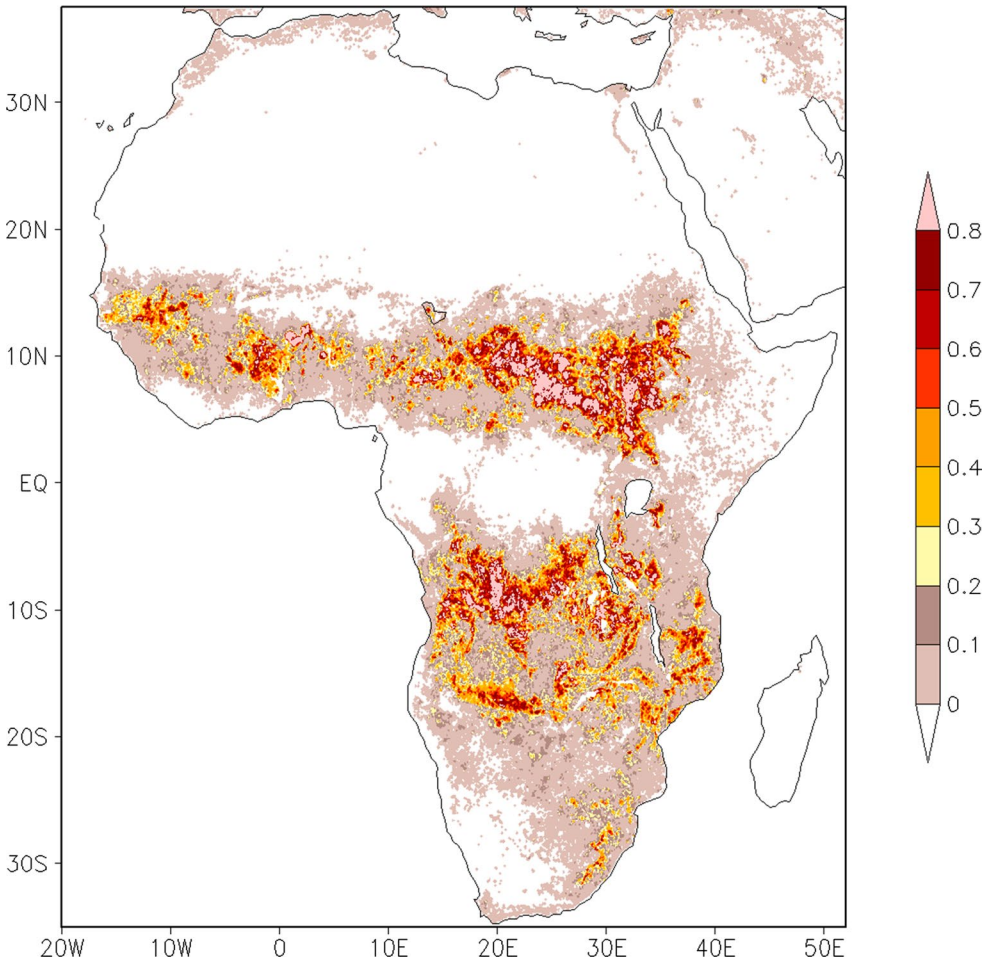

Fig. 3 2002–2011 annual mean burned area fraction calculated based on MODIS approximate date of burning product aggregated from the native resolution to regional model grid

Table 1 Cover fraction, annual burned area fraction, survival rate, and albedo change during wildfire season (Oct–Mar) for the major land cover types averaged over area A (Fig. 1 inset)

Land cover type	Area (%)	Annual burned area fraction (%)	Survival rate (%)	Annual change in albedo (%)
Rainforests	13.3	0.4	75.0	1.3
Other forests	5.7	4.6	75.0	2.9
Savannas	43.6	28.4	15.0	7.3
Grasslands	6.3	7.9	0.0	3.5
Shrublands	23.6	5.9	0.0	3.0
Croplands	2.0	6.8	0.0	0.9

Shrublands include shrubs with and without ground cover

and lastly croplands (2.0 %). Other (non-rainforest) forests form the boundary between rainforest and savanna. The approximate amount of burned area for each of these land cover types are 28.4, 5.9, 0.4, 7.9, 4.6, and 6.8 % respectively. Therefore, in term of overall spatial extent, most of burned areas are originally savannas, followed by shrublands and grasslands. The West African rainforest is only weakly impacted by burning despite occupying about 13 % of the area.

2.3 Experimental design

To investigate the impact of burned area on the monthly climate over the Sahel, two sets of experiments were carried out. In one set, undisturbed land surface properties namely leaf area index (LAI), and vegetation cover taken from Fourier-adjusted, sensor and solar zenith angle corrected, interpolated, reconstructed dataset (FASIR, Los et al. 2000) were used as surface boundary conditions and

updated daily in the simulations. Wildfire effects were not included in this set of simulations, which will be referred as unburned (control) experiment.

In the burned area experiments, LAI and vegetation cover data were altered based on the burned area fraction described above and on the prescribed survival rate of the vegetation type. Vegetation cover was updated every 24 h of simulation following Eq. 1, where VC_u, FBA, and SR represent the original (unburned) vegetation cover, the fractional burned area, and the survival rate, respectively. A similar equation was used to alter the LAI. The resulting vegetation deterioration, thus, depends not only on the fraction of burned area but also upon vegetation survivorship. The vegetation survival rates used in this study are similar to those used in the study by Thonicke et al. (2001) adjusted to the WRF-NMM/SSiB2's land cover types (see Table 1).

$$VC = VC_U[1 - FBA \times (1 - SR)] \quad (1)$$

In addition to altering the vegetation, soil reflectance was lowered based on the same amount of burned area fraction and survival rate to simulate the effect of ash and charcoal depositions associated with wildfires (Govaerts et al. 2002; Samain et al. 2008). Ground darkening was maintained for a certain period, after which the soil albedo was returned to its normal (unburned) values to mimic the action of char removal by wind and precipitation. Several sensitivity tests were performed to examine the impact of the darkening time scale, including permanent darkening (no char removal) and no charcoal deposition simulations.

These tests indicated the model to be nearly insensitive to removal time of <10 days, while permanent darkening generated unrealistic results (not shown). For the purposes on this study and due to the limited number of observation on charcoal removal time, all burned simulations were carried out with a charcoal removal period of 10 days, during which shortwave and near-infrared ground albedo was arbitrarily set to 0.1 over the burned fraction of the grid cell only. This value is consistent with recent post-fire albedo found in Africa by Govaerts et al. (2002). Also, the ten-day removal period is corroborated by the results presented in the previously mentioned work by Samain et al. (2008).

A five-member ensemble of simulations was performed for the unburned and burned experiments to reduce uncertainties associated with the initial conditions. The ensemble members were initialized at 00z 27, 28, 29, 30 September and 01 October 2010 and ended at 00z 01 October 2011. No form of interior nudging was utilized for simulations, which were carried out continuously without any restarts. NCEP-DOE Reanalysis 2 (Kanamitsu et al. 2002) was used as atmospheric initial and boundary conditions in all simulations, as well as sea surface temperature information. All reported results are based on the 5-member ensemble averages of the experiments.

3 Results

3.1 Control simulations

Before the impact of burned areas on the Sahelian precipitation and surface climate is explored, we first evaluate the regional model's control simulations. This evaluation is necessary since it provides a benchmark for assessing the impact of burned areas. In addition, there have not been any previous publications describing North African climate results from the WRF-NMM/SSiB2 regional model. Sub-Saharan precipitation is primarily controlled by the West African monsoon system (Xue et al. 2010b). The monsoon circulation is forced and primarily maintained by land-sea thermal contrast. Following the seasonal northward migration of the Inter-tropical Convergence Zone, the monsoon develops during the spring months and moves northward during the following months (Sultan and Janicot 2003).

On average, rainfall starts in the Sahel in May and continues through the summer months. In August, the monsoon brings precipitation to its northernmost locations and then starts to withdraw south in September. The seasonal movement of the monsoon described above is evident in the Tropical Rainfall Measuring Mission (TRMM) merged microwave/infrared precipitation estimate dataset (Huffman et al. 2007) with its northernmost reach in August and southernmost position in January (Fig. 4). Monthly average precipitation over the area A, which comprises the main region affected by the West African monsoon (Fig. 1 inset), indicates that the wettest month is September with 6.3 mm day^{-1}, while the driest is January with 0.3 mm day^{-1}. WRF-NMM/SSiB2 is able to capture the monthly movement of the West African monsoon (Fig. 5). Similar to the TRMM, the model simulates the southernmost and northernmost positions of the monsoonal rainfall band in January and August, respectively. On average, the wettest month in the simulation is September with 7.1 mm day^{-1}, while the driest is January with 0.7 mm day^{-1}.

The model, however, tends to mainly overestimate the monthly precipitation in some areas. Simulation results show areas of intense precipitation over land, especially near the Guinean Gulf coast and in the highlands of western Sudan during the summer months, which are not seen in the TRMM estimates (Fig. 5). Modeled annual mean precipitation bias and root-mean-squared error calculated based on TRMM observations are approximately 1.1 and 3.0 mm day^{-1} respectively. Most of wet bias over land is located in eastern Sahel east of 10°W, especially

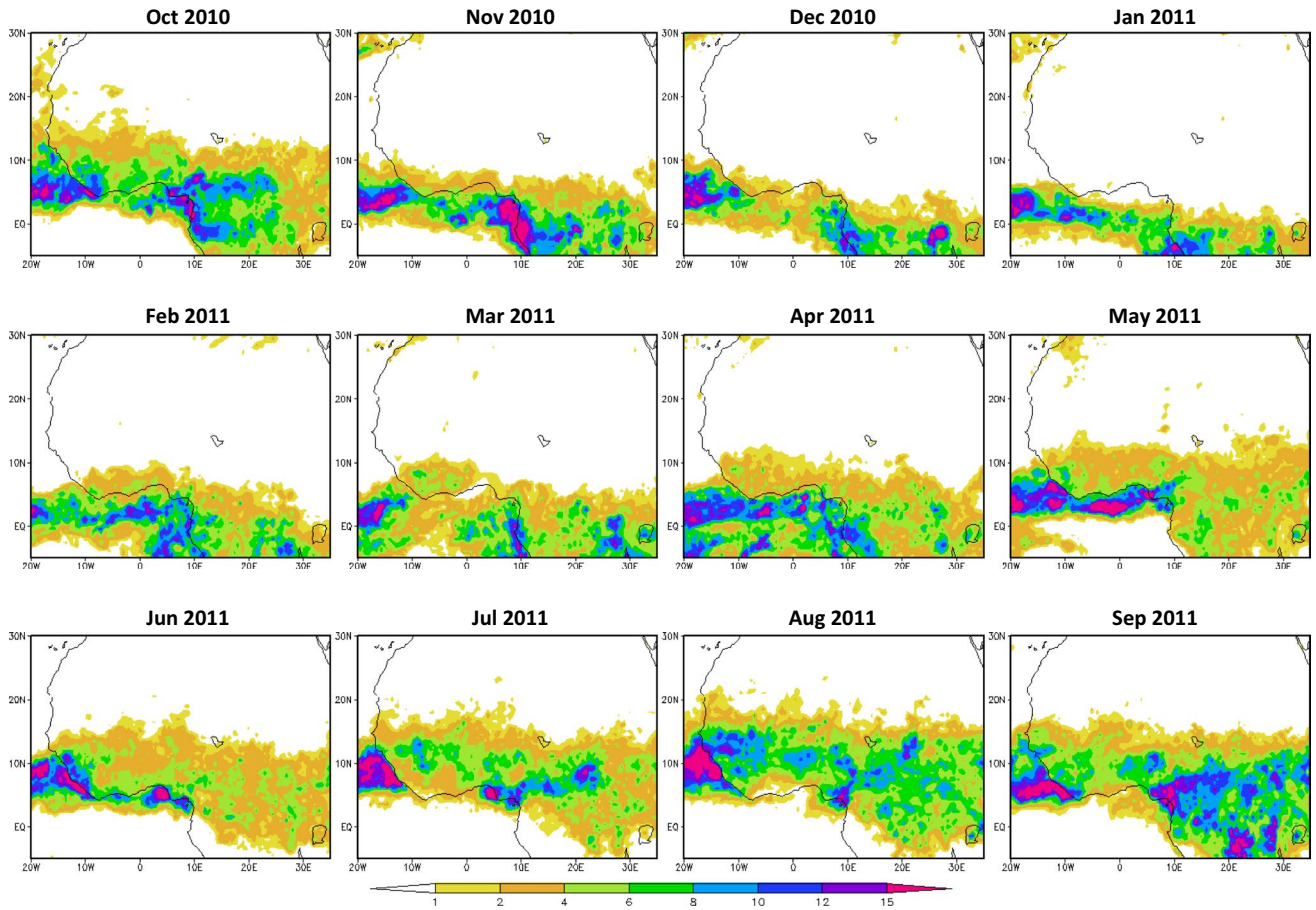

Fig. 4 TRMM 3B42 monthly mean precipitation estimates from Oct 2010 to Sep 2011 (mm day^{-1})

in June and August when precipitation biases are above 8 mm day^{-1} in some areas within the monsoonal band.

A large area of negative bias is located in the southwestern section of the domain in September, which may be linked to a slower-than-observed monsoon withdrawal. Due to the lack of in situ precipitation observations in these parts of Africa and the limitations associated with satellite-based precipitation estimates assimilated into the TRMM product, it is difficult to realistically assess model biases in these areas. Nonetheless, results indicate that the model can reasonably simulate the precipitation temporal and spatial patterns over Sub-Saharan Africa.

Monthly near-surface air temperature results provide a good indicator of the model's performance in simulating land/atmosphere interactions such as canopy radiation transfer and land surface energy balance. Model results are compared against the Climate Anomaly Monitoring System (CAMS) monthly surface air temperature product (Fan and van den Dool 2008) (Fig. 6). Most of the annual variability is concentrated over the Sahara desert, where surface air temperatures vary by as much as 25 °C in some areas. Another interesting pattern is the sharp temperature gradient in the Sahel in the summer months. Denser vegetation keeps temperatures from varying much in the south, where it remains around 20–25 °C yearlong.

The evolution of the monsoon is intimately linked to surface temperature variability modes in Northern Africa and their accurate representation in models is crucial for accurate simulations of monsoon evolution (Xue et al. 2010b). The northward movement of monsoonal precipitation is associated with the weakening of the warmer temperature band over the Sahel (Sahel mode) and the enhancing of warmer temperatures over the Sahara desert (Sahara mode), which in turn enhances the meridional temperature gradient in the region during the monsoon onset.

In general, the WRF-NMM/SSiB2 can simulate the main features of monthly temperature fields over the area of study, including the main seasonal variability modes described above (Fig. 7). The model simulates the winter-to-summer transition in the Sahara where annual temperature variability is largest. Further south, where vegetation is denser, modeled temperatures are within observed ranges. There are positive biases especially over Western Sahara, where modeled temperatures are about 6 °C higher than

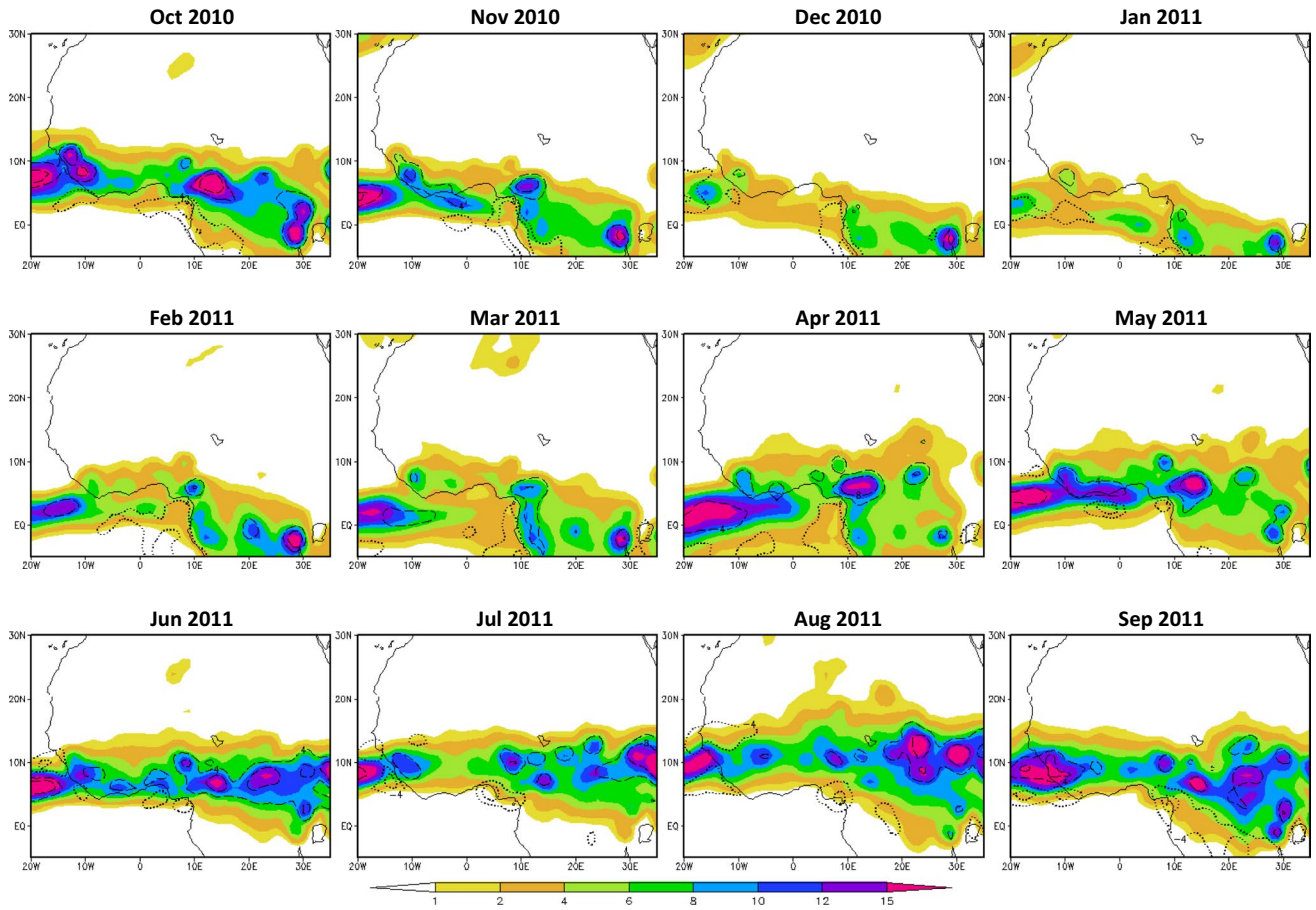

Fig. 5 Modeled monthly precipitation mean (*shaded*) and bias (*contour*) from Oct 2010 to Sep 2011 (mm day^{-1}). Precipitation bias is represented by *dotted* (-2 and -4 mm day^{-1}) and *dashed* ($+2$ and $+4$ mm day^{-1}) *contour lines*

observed in some areas. However, as in the case of precipitation, the lack of in situ measurement in these areas limits an accurate bias assessment there. Little bias is observed in the cooler months between November and March. The mean monthly temperature bias and root-mean-squared error in the area A based on CAMS observations are equal to 0.1 and 1.4 °C, respectively.

The zonal circulation over the study area is marked by large differences between winter and summer as indicated by pressure-latitude cross-sections of monthly zonal wind from the Reanalysis product (Fig. 8). From November to February, the mean upper-level zonal circulation is characterized by strong westerly winds north of 10°N, which extend down to the mid-levels of the troposphere. South of 10°N, winds are weaker and mostly from east at mid-levels and from west near the surface. As the wet months approach, the upper-level westerlies give way to easterly winds (the tropical easterly jet), which reach a maximum in August. Concurrently, the African mid-level easterly jet (between 600 and 700 hPa) and the lower-level tropical westerly jet (below 800 hPa) become more apparent (Fig. 8). These three jets are key features associated with the West African monsoon evolution and are linked to the position and intensity of the monsoon precipitation band (Sultan and Janicot 2003; Xue et al. 2010b).

The model simulates reasonably well the wind circulation over northern and western Africa, including the African mid-level easterly and upper-level westerly jets, as well as the onshore low-level flow responsible for supplying moisture to the monsoonal precipitation (Fig. 9). It also captures the predominant upper and mid-level westerlies during the dry season over northern Sahel and Sahara desert, observed in the Reanalysis product. Nevertheless, the model tends to overestimate of the onshore low-level flow and underestimate the mid-level African easterly jet intensities during the monsoon seasonal, which may explain the wet biases simulated over parts of the Sahel from June to August 2011 (Fig. 5). Overall, however, the modeled wind circulation is consistent with the Reanalysis product.

The results reveal that by and large, the WRF-NMM/SSiB2 can reliably simulate the seasonal climate of northern Africa and provide a reasonable basis against which to

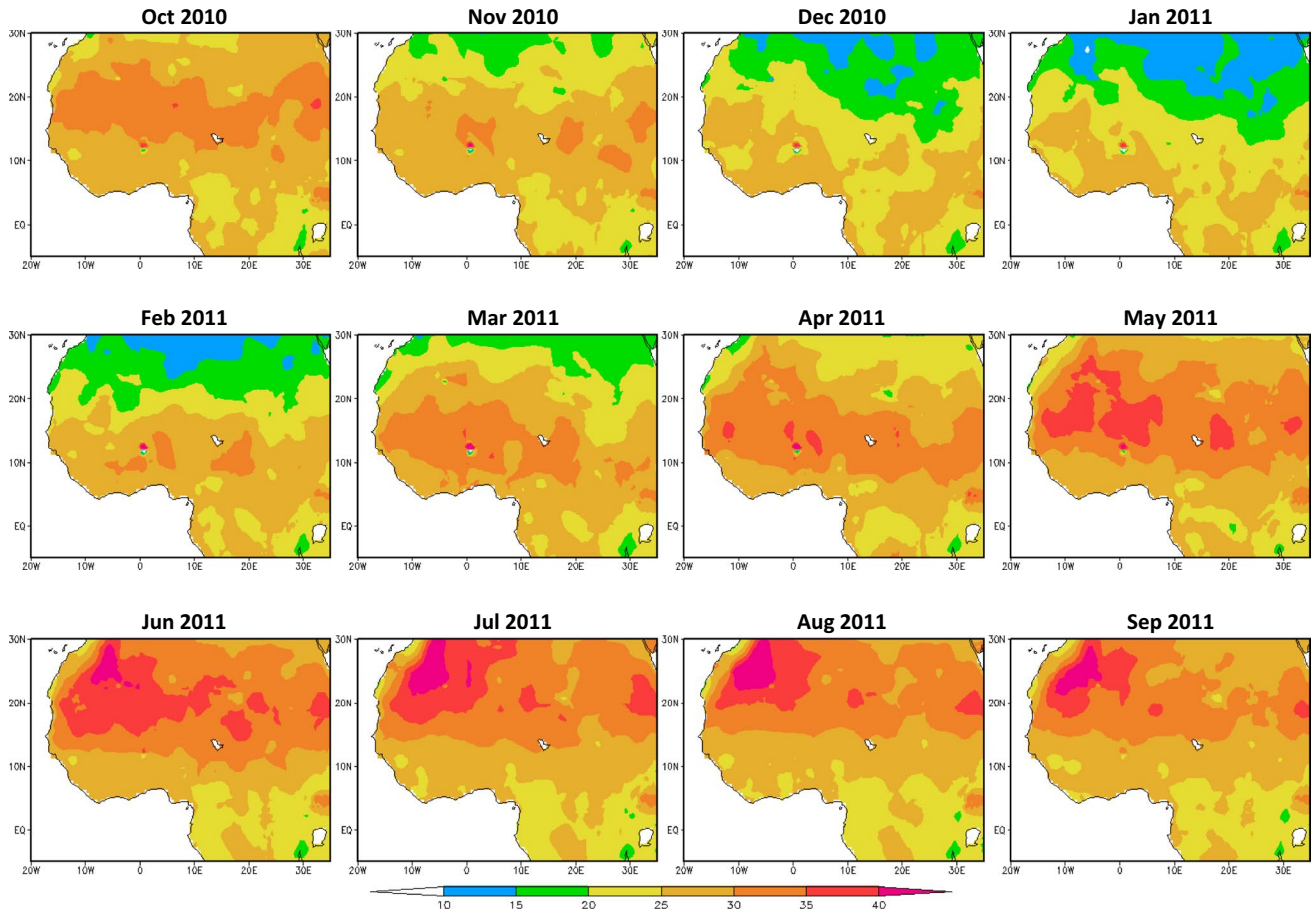

Fig. 6 CAMS monthly mean surface air temperature observations from Oct 2010 to Sep 2011 (°C)

estimate the impact of fractional burned area in the region's energy balance and precipitation.

3.2 Burned area impact

In the MODIS data, the main contribution to burnt area fraction totals (Fig. 3) comes during late fall, winter, and early spring. Burned areas start to become more widespread in October and by November three distinct areas of burn scars can be seen: one over the eastern Sahel between 15°E and 35°E, and two others slightly farther north over the western Sahel between the Atlantic Coast and 5°W (Fig. 10). The burning fraction reaches a peak in December, when a nearly continuous band of high burned area fraction extends from the Atlantic Ocean coast to Sudan in eastern Sahel. Several parts of sub-Saharan Africa exhibit burned fraction above 25 % during this month. Intense burning continues in January but with less intensity and starts to substantially weaken by February and March. Due to the monsoon, summer experiences nearly no fire activity and thus little burned fraction is registered in the region.

In the Sahel, under undisturbed conditions, changes to surface albedo are often associated with changes to the top soil water content and vegetation annual phenological cycle. As a result, maximum average albedo values are often reached by the end of dry season, followed by a slow decrease during the monsoon season. Under fire-disturbed conditions, two other distinct processes (vegetation alteration associated with burning and ground darkening resulting from char deposition) play the primary role in albedo change.

Therefore, during the dry season, as vegetation degradation increases with increasing burned areas, larger and larger portions of bare ground become directly exposed to solar incoming radiation. Despite the brief ground darkening from ash and charcoal deposition following wildfires, the model simulations indicate that the resultant effect is to increase the monthly average surface albedo in the areas where bare ground albedo is higher than the overlying vegetation reflectance.

In the model, savanna experiences the largest albedo change, with 7.3 % albedo increase (Table 1). Shrublands,

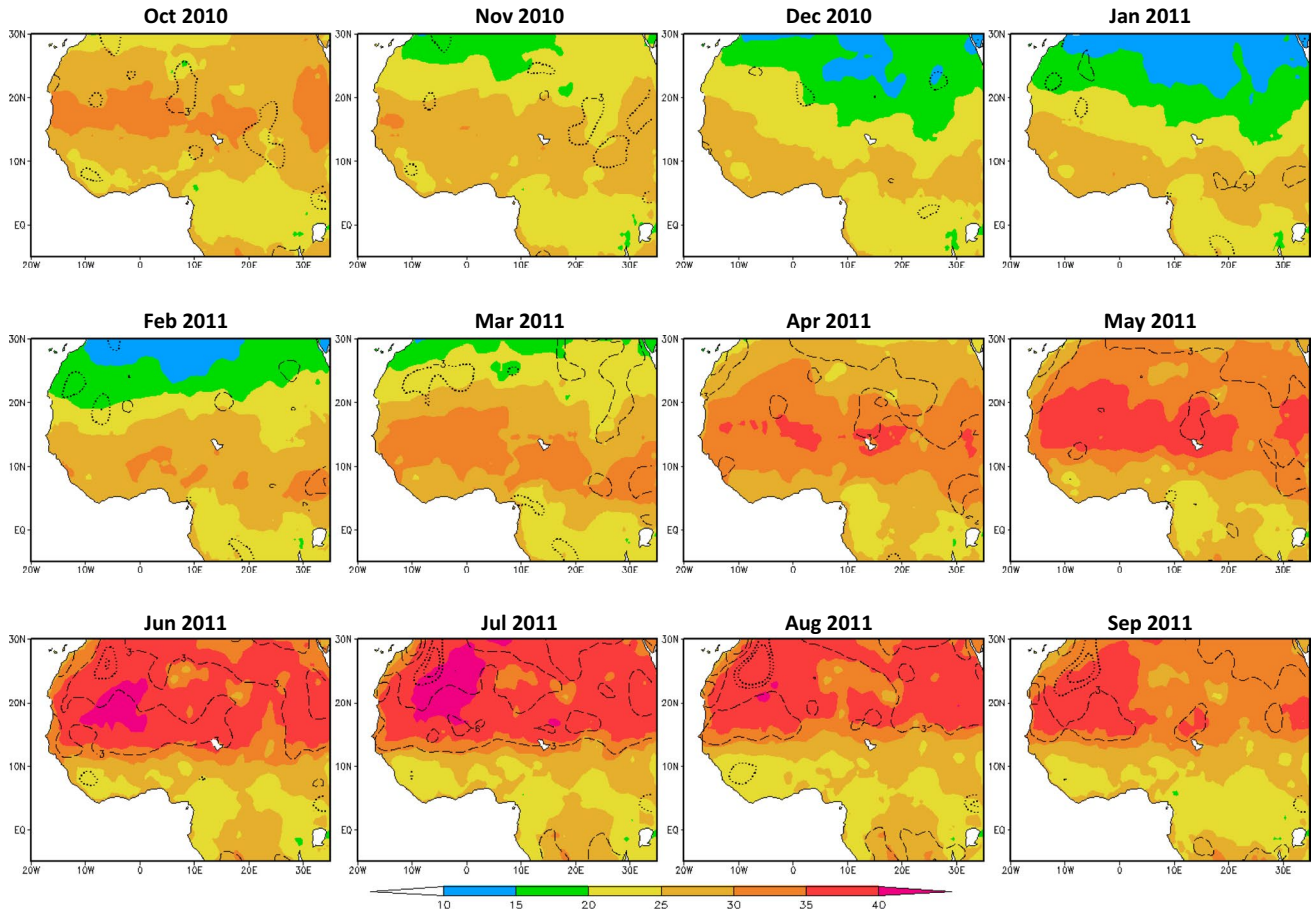

Fig. 7 Modeled monthly surface-air temperature mean and bias from Oct 2010 to Sep 2011 (°C). Temperature bias is represented by *dotted* (−3 and −6 °C) and by *dashed* (+3 and +6 °C) *contour lines*

grasslands, and dry forests exhibit approximately 3.5, 3.0, and 2.9 % of albedo increase due to wildfire-induced land degradation compared to unburned experiments. On the other hand, cropland and rainforests show negligible changes. Averaged over the entire area A, the wildfire-season land albedo is increased by about 6.3 %.

Changes in the surface radiation balance (Figs. 11, 12a) are consistent with the albedo changes in the burned areas (Fig. 10). The changes in albedo and net radiation are small in early fall. By December, a large area of decreased net radiation appears in eastern Sahel, which becomes larger and more intense through the winter and spring seasons. The areal extent of surface net radiation decrease peaks in February and March over the burned areas (Fig. 12a). Figures 11 and 12 only include grid points where the net radiation differences are significant at a 90 % level of confidence.

There are positive surface net radiation changes over the West African rainforest during winter and spring months (Fig. 11). Since virtually no burn occurs in this region, such an impact is not a directly result of wildfire. The increase in net radiation over the rainforest zone is likely a result of increased insolation associated with reduced cloud cover and precipitation over the area, which will be discussed later. As the rainy season starts, the impact of burned area on surface radiation balance weakens; however, negative differences (lower net radiation in the burned simulations) still dominate throughout the Sahel, central Africa and parts of the Sahara.

As the amount of net radiation at surface decreases due to burning-induced land condition deterioration, so should the amount of energy transported from surface to the atmosphere through sensible and latent heat fluxes. Partitioning between these two processes is complex and depends on the atmospheric surface layer conditions and ground cover conditions. The impact of burned area on monthly net radiation, sensible and latent heat fluxes averaged over burned areas within the area A is shown in Fig. 12. February and March are the months with the largest net radiation drops; with approximately 10 W m^{-2} reduction compared to the control simulations.

During the dry season months, between October 2010 and March 2011, most of the burned area's simulated net

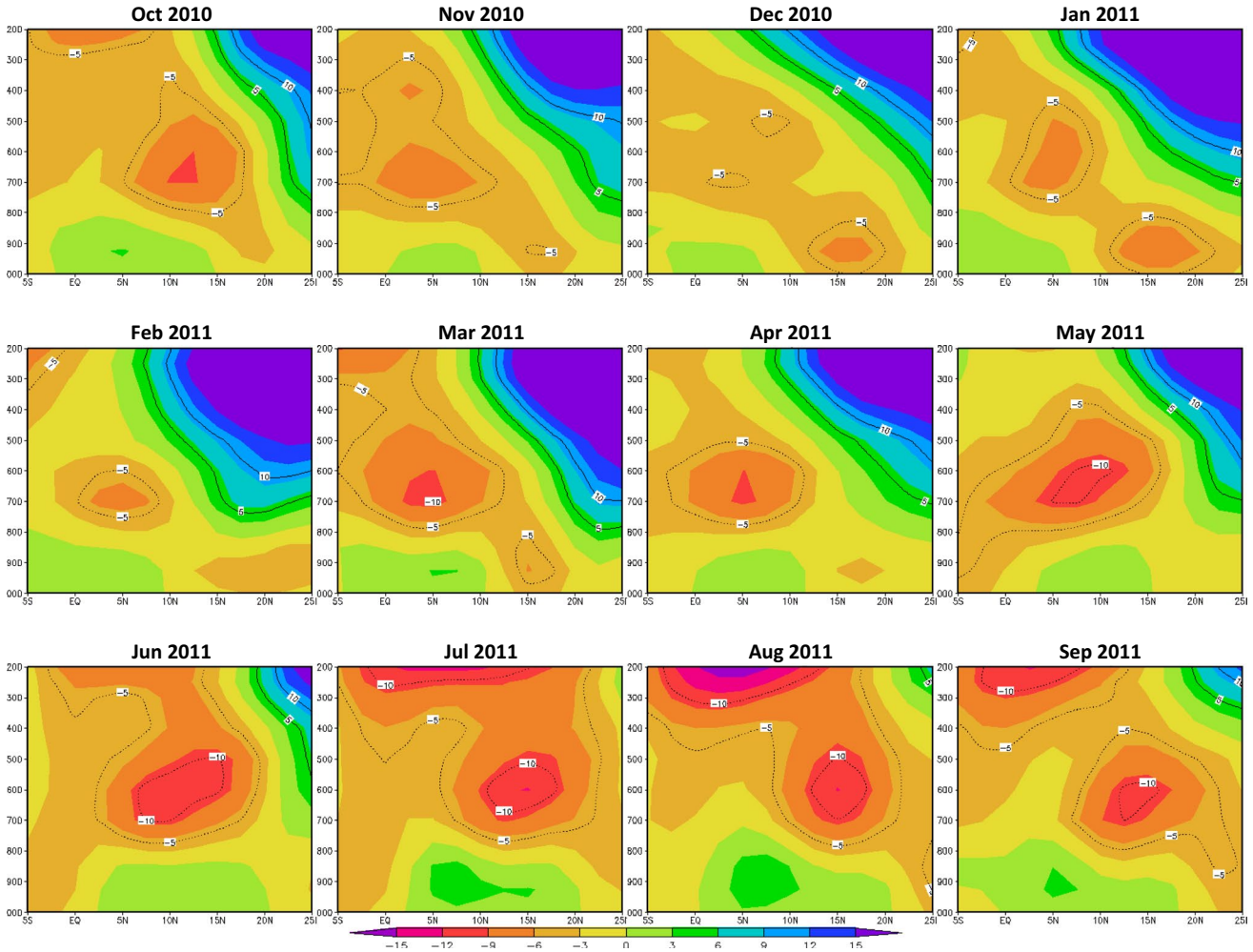

Fig. 8 Pressure-latitude cross-sections of Reanalysis-2 monthly-averaged zonal wind between longitudes 10°E and 10°W from Oct 2010 to Sep 2011 (m s^{-1})

energy decrease contributes to the reduction in surface sensible heat flux to atmosphere. Decreases are seen in latent heat in these months; however more than 80 % of total net radiation reduction is being directed into less sensible heat to the atmosphere. During the monsoon pre-onset and onset months of April and May, on the other hand, the impact on latent heat flux becomes larger than on sensible heat flux. Nearly all net radiation decrease results in less surface evapotranspiration in these months. A similar behavior takes place during the peak monsoonal months; however, the reduction of net radiation is small (<5.0 W m^{-2}) during the rainy months. Results indicate a transition in the burned area impact on surface sensible/latent energy partitioning from March through May. This timing coincides with the pre-onset and onset stage of the West African monsoon in the area (Xue et al. 2010b).

The impact of burned areas on monthly rainfall over Sub-Saharan Africa is shown in Fig. 13, which displays the precipitation difference between burned and unburned experiments. A mask was applied to this figure so that only differences within a *T* test 90 % confidence interval are shown. As with net radiation, the impact on precipitation is weaker in late fall and early winter and then intensified through late winter and spring months. However, the impact on precipitation seems more widespread.

Broad areas with negative precipitation differences move slowly northward from January to May 2011. By February, a band of reduced extends from the Atlantic Coast eastward to Lake Victoria, with some locations showing precipitation decrease of more than 1 mm day^{-1} (Fig. 13). A comparison with Fig. 10 reveals that this band of precipitation differences is located south and west of the burned areas for the month. In May, a somewhat homogeneous negative precipitation band covers large continental areas along the 5°N parallel.

The pattern of rainfall impact during the rainy-season months shows a more complex structure with a large dipole

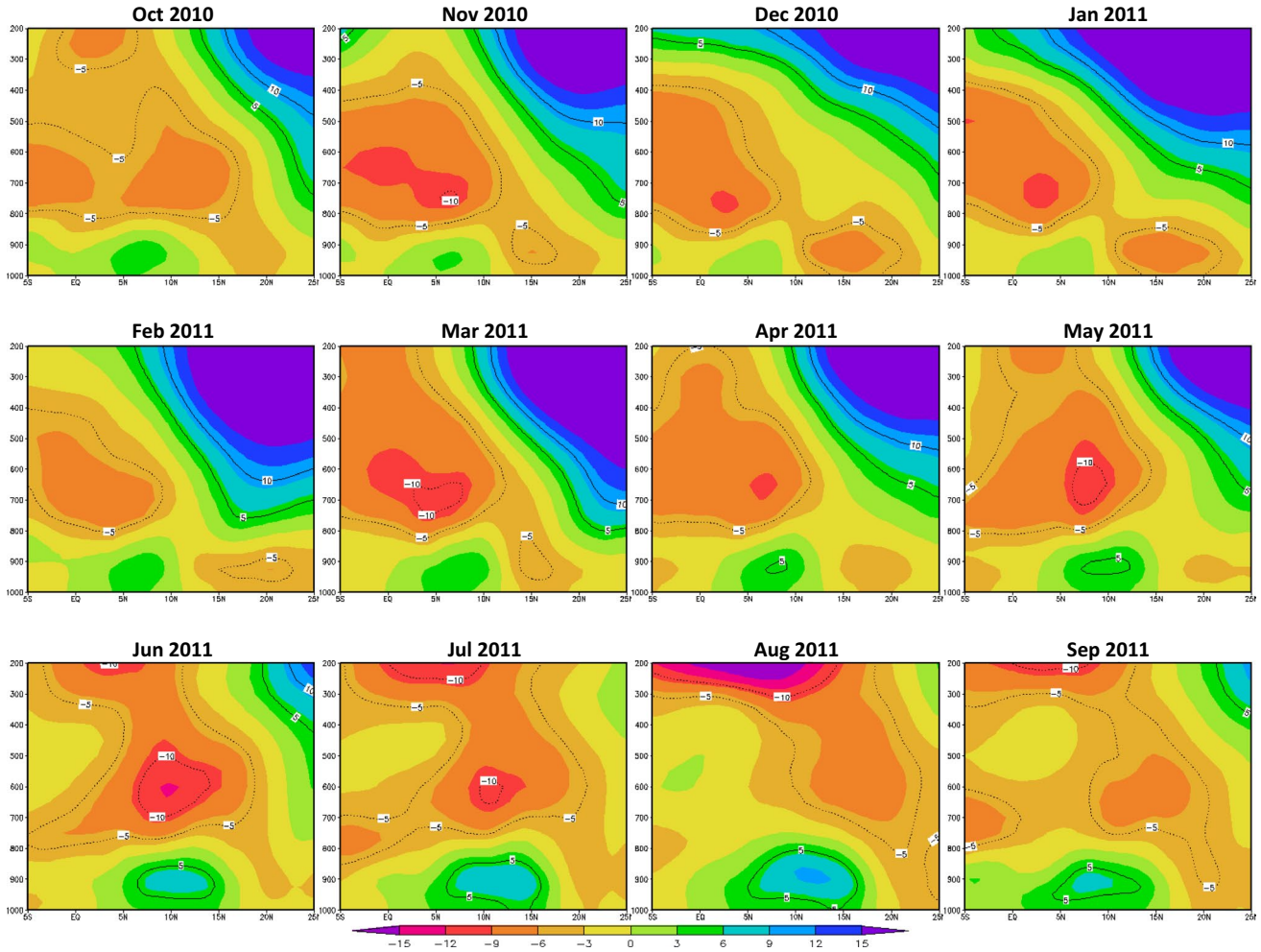

Fig. 9 Pressure-latitude cross-section of modeled monthly-averaged zonal wind between longitudes 10°E and 10°W from Oct 2010 to Sep 2011 (m s^{-1})

pattern across the region during June–September. The positive areas are mostly located to the south of 10°N in June with negative precipitation areas to the south and north. In July and August, the pattern seems to reverse; the negative precipitation again covers most area in Sahel with positive to the south and north. The spatial pattern in September is similar to June, though the dipole is less organized then. By and large, Fig. 13 shows that the impact of burned area on precipitation is not limited to the burned areas themselves; significant precipitation change occurs over the West Africa's tropical rainforest and over the shrublands of northern Sahel where little to no burned area exists.

To further examine the effect of wildfire vegetation alteration on West African monsoon evolution, time-latitude diagram of 10-day running mean precipitation difference between burned and unburned experiments from Nov 2010 to Sep 2011 in the area A was calculated (Fig. 14a). Overall, the diagram shows negative precipitation differences between 5°S and 5°N staring in late November and continuing through late August. Three months with the largest precipitation reduction (February, April, and August) are apparent in Fig. 14a and consistent with Fig. 13. The first precipitation reduction maximum occurs in February when differences larger than 1 mm day^{-1} are seen. Most of this event takes place over the West African rainforest to the south of the main burned areas.

The band of negative precipitation becomes less intense in March as it starts to move northward. In late April, it re-intensifies north of the Equator (second maximum) as it continuous to progress northward. It reaches its northernmost position in early August at nearly 10°N, when the third reduction maximum in precipitation appears, then it starts to shift southward as the monsoon withdraws from the region. When compared to TRMM estimates (Fig. 4) the time-latitude diagram reveals that burned-area-induced precipitation reduction follows the northward progression of the West Africa monsoon, and suggests a weakening in its evolution especially during the pre-onset and onset stage

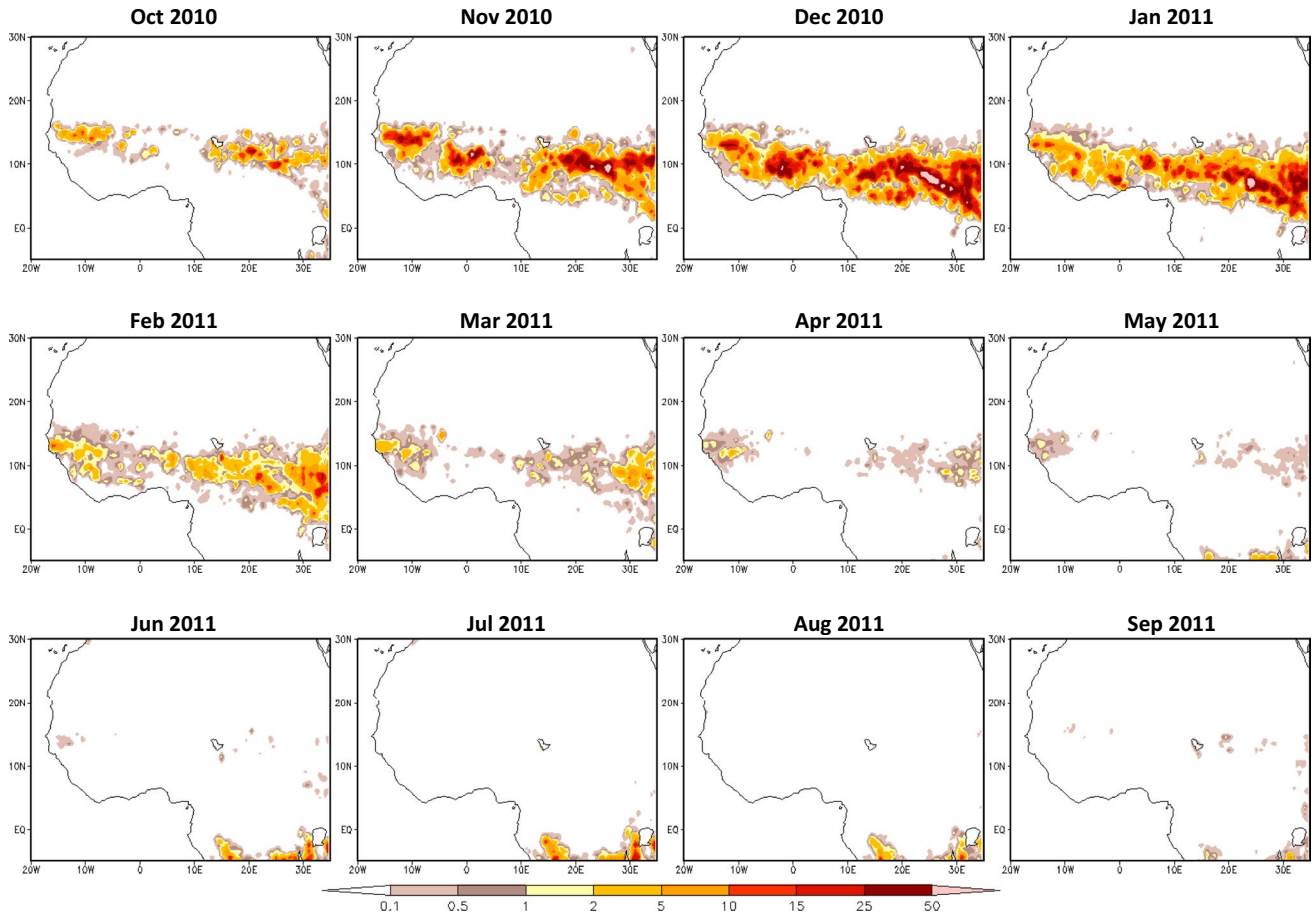

Fig. 10 Monthly burned area fraction from Oct 2010 to Sep 2011 over West Africa (%)

months (Xue et al. 2010b). A narrow band of positive precipitation difference is located to the south of the larger precipitation decrease belt and starts to emerge from January to early April. During late summer, positive precipitation differences can also be seen north of 10°N as well as along the Equator.

Time-latitude diagrams were also calculated for surface evapotranspiration and atmospheric moisture flux convergence (MFC), which are the main components to the atmospheric water balance at monthly scales (Fig. 14b, c). By and large, changes in precipitation result from changes in atmospheric MFC component. On average, MFC accounted for more than 90 % of the precipitation changes in the area A and its evolution pattern resembles closely that of precipitation. The three largest precipitation reduction occurrences (Fig. 14a) are associated with distinct atmospheric MFC decreases, which are evident in Fig. 14c. Evapotranspiration changes are minimal and only marginally relevant in February, early March, and May, when it contributes to approximately 10 % of the precipitation reduction (Fig. 14b). Unlike atmospheric MFC, evapotranspiration changes are nearly always negative.

The consistency between precipitation and atmospheric MFC changes indicates that surface energy balance adjustment resultant from burned areas induce wind circulation changes, which contribute to the precipitation changes. Overall, Figs. 13 and 14 indicate that these circulation changes work to delay the northward progression of the monsoon during its pre-onset and onset phases causing precipitation to decrease at the leading edge of the monsoonal band; and to intensify south of the monsoonal band. During summer, results show strengthening of atmospheric MFC due north and south of the main burned areas causing precipitation to increase there. This pattern is especially evident in August when enhanced precipitation is observed northward of 10°N and southward over the West African rainforest in the simulations (Fig. 14a). The large reduction in atmospheric MFC positioned around 18°N in September is not associated with any precipitation changes, as it is located too far north from the monsoonal rainfall band (Fig. 5). Further consideration on the mechanisms associated with burned-area-induce circulation and precipitation changes will be given in the next section.

Monthly and annual mean relative precipitation differences for the major land cover types were calculated over

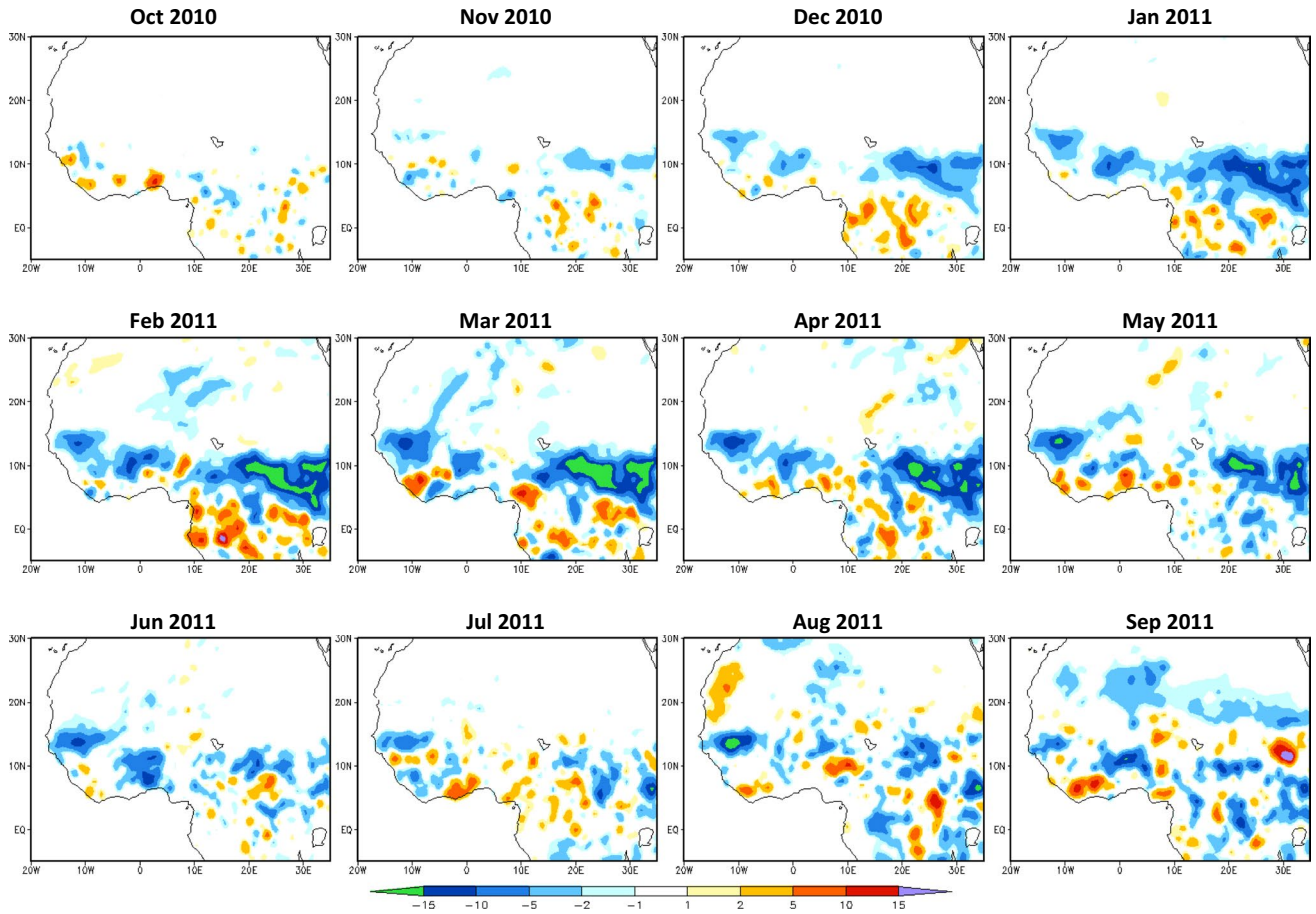

Fig. 11 Monthly surface net radiation differences between burned and unburned simulations from Oct 2010 to Sep 2011 (W m^{-2})

the area A (Table 2). Only grid points with differences at 90 % significance level were used in the calculation. The largest relative impact is for areas covered by savanna, followed by rainforests, other forests, and shrublands; with 3.8, 3.3, 2.6 and 2.1 % drop in annual precipitation each respectively. Despite experiencing little to no wildfires, forested land experiences significant decrease in rainfall, especially in February when it rained nearly 19.2 % less than in the undisturbed experiment over the West African rainforest (Fig. 13). That same month, savanna receives approximately 14 % less than its unburned rainfall total. The annual mean precipitation change for the entire area A is approximately −3.2 %.

4 Discussion

Differences in surface albedo between the burned and unburned sets of simulations depend primarily on three distinct processes; changes in vegetation conditions, ground darkening resulting from charcoal deposition associated with burning, and changes in top soil moisture content. The combined impact of these processes on the surface radiation balance (Fig. 11) reduced the amount of energy available for turbulent fluxes in the burned areas, thus lessening the amount of heat and moisture at lower levels of the troposphere. During the dry season (November 2010 to March 2011) most of this energy reduction over burned areas was accounted for by a decrease in monthly sensible heat flux to the atmosphere (Fig. 12). This partitioning pattern changed to most of reduction being directed to evapotranspiration in April and May which then continues, at weaker intensities, through the rainy months.

Burned-area-induced precipitation impact was widespread and mostly negative in the area of study. The atmospheric water balance in the region revealed that changes in atmospheric MFC in the burned area experiments were consistent with changes in precipitation (Fig. 14). The impact on atmospheric MFC was a dominant factor compared to surface evapotranspiration (Fig. 14b, c) indicating significant changes in wind circulation and moisture advection resultant from burned area degradation in and around the region.

Based on these results, we hypothesize that the aforementioned processes, namely the weakening of turbulent

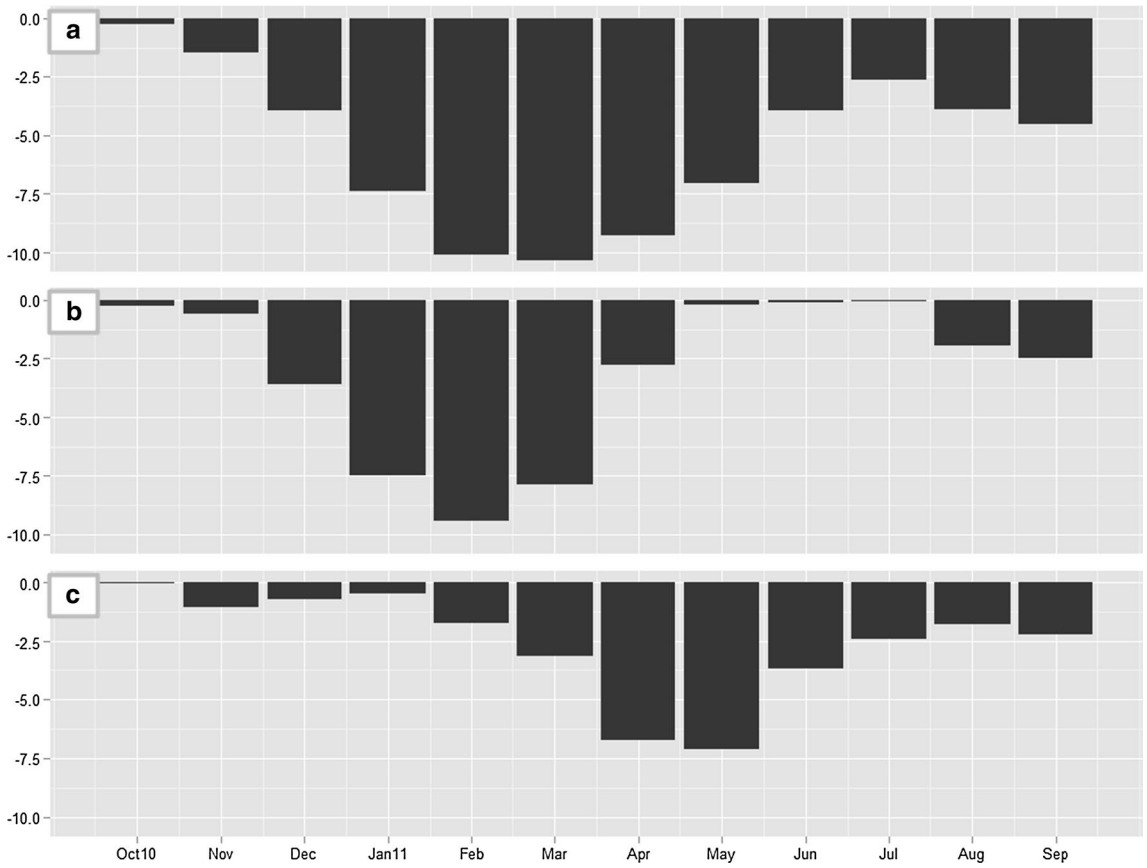

Fig. 12 Monthly mean differences between burned and unburned simulations for **a** surface net radiation, **b** surface sensible heat flux, and **c** surface latent heat flux averaged over burned areas within the area A (W m^{-2})

heat fluxes and reduction of atmospheric MFC, worked together to reduce precipitation in Sub-Saharan Africa by enhancing subsidence and rendering the troposphere convectively more stable in the burned area experiments. To confirm this hypothesis we examine the impact of burned areas on the mid-tropospheric vertical pressure velocity in the area A (Fig. 15a, b). Unburned 10-day running mean 500 hPa vertical pressure velocity time-latitude diagram shows the bulk of upward motion south of the Equator from November through April (Fig. 15a). A sharp shift northward takes place in April signaling the onset of the monsoon in the Sahel. Upward motion band then intensifies through the summer reaching maximum intensity in July and August, after which it starts to move southward. Weak subsidence is observed to the north and south of the main upward motion band. It is evident from the figure that average mid-tropospheric upward motion follows the monsoonal precipitation evolution.

The burned-area impact on vertical mid-tropospheric circulation is shown in Fig. 15b. Overall, it reveals a weakening of upward motion during the pre-onset, onset, and mature stages of the monsoon development as a result of decreased atmospheric heating. Maxima weakening episodes occur in February, May and August, which is consistent with the largest precipitation changes. From December to April, most of the impact was located slightly north of the strong upward motion band, which indicates the intensification of pre-monsoon subsidence in the Sahel. The resulting unfavorable conditions for convective activity in the region hindered the monsoon progression through the area and enhanced precipitation to the south.

Similar conditions may also explain the changes in atmospheric MFC and precipitation during the spring months. Intensification of large-scale subsidence over sub-Saharan Africa has been shown to be correlated with the decreasing precipitation trends in the Sahel (Xue and Shukla 1993). During summer, most of the negative impact on vertical circulation is within the monsoonal band, indicating a general weakening of convective activity of the monsoon. By mid-August, two relative-upward centers are observed flanking the main relative negative difference band in the simulations (Fig. 15b). It is possible that these relative-upward cells form in response to the widespread relative-negative larger cell between 4° N and 12° N. These

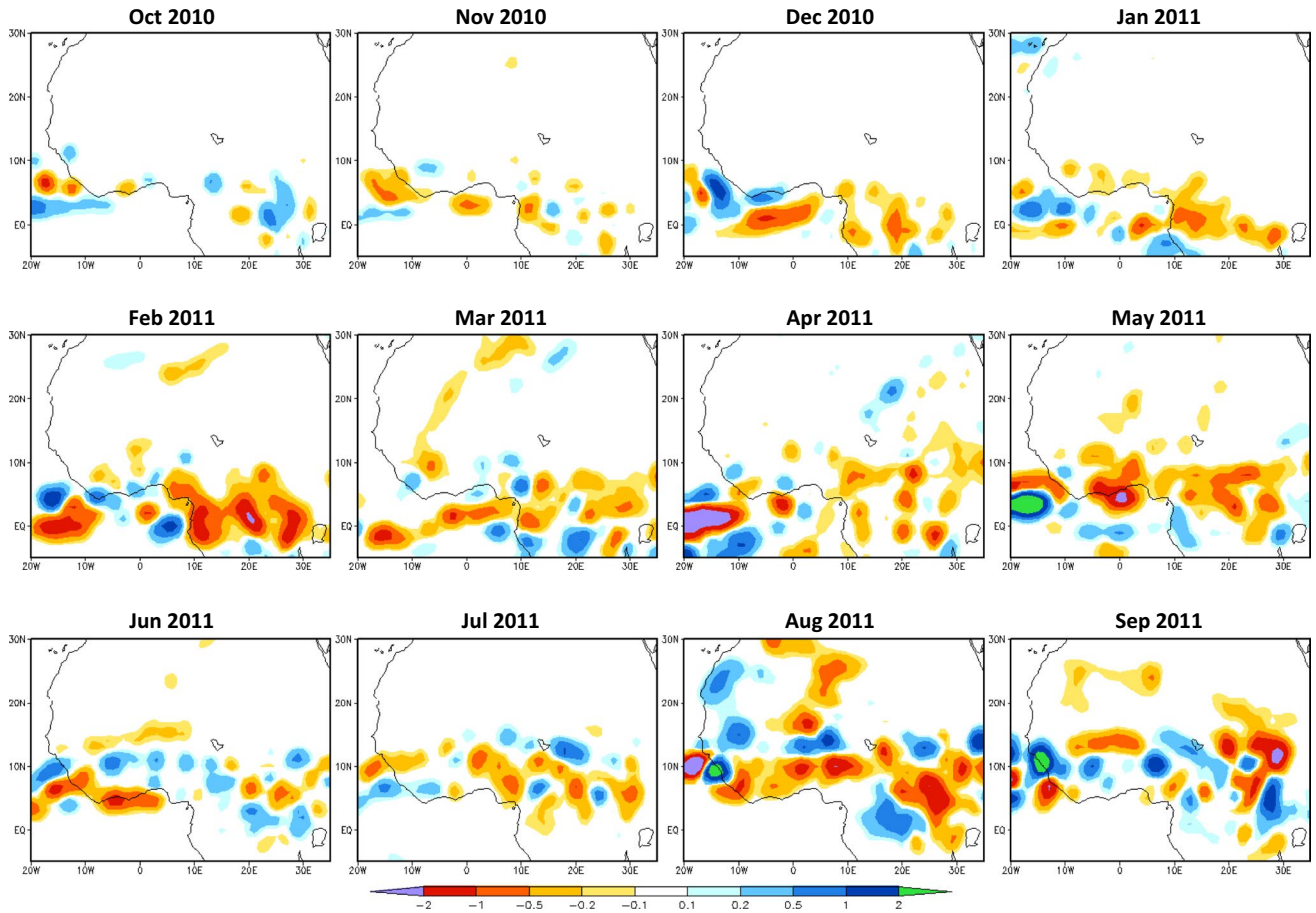

Fig. 13 Monthly mean precipitation differences between burned and unburned simulations from October 2010 to September 2011 (mm day^{-1})

relative-upward cells warranted favorable convective conditions to develop outside the main impacted areas and explain the increase in atmospheric MFC and precipitation to the north and south of the monsoon band in August (Figs. 13, 14).

Additionally, we expect that if the precipitation reduction observed in the burned area experiments were indeed caused by the lessening of convective instability, there should be a decrease in the number of convective precipitation events in the area. To examine this impact we calculated the average observed and modeled precipitation energy in the area A for the study period based on daily precipitation totals. Precipitation energy provides a measure of the number of precipitation events exceeding a given threshold integrated over an area (De Sales and Xue 2011).

Considering that frequent precipitation events exceed low rainfall thresholds, low thresholds are usually associated with high precipitation energy. As the threshold increases, more frequent and weaker precipitation events are disregarded, resulting in low precipitation energy for more intense events for the area. Figure 16 shows the daily precipitation energy distribution from TRMM estimates (black line), as well as for unburned and burned experiments (blue and red lines, respectively) for the area A. Since daily precipitation is used for the calculation, we can assume that high-threshold events are associated with intense convective precipitation events, which usually last for <24 h. The positive bias previously discussed in simulated precipitation (Fig. 5) is also evident in daily precipitation energy distribution (Fig. 16), as both simulation experiments exhibit higher counts of precipitation events for threshold between 0.01 and 1 mm day^{-1}, as well as for thresholds above 3 mm day^{-1}.

The difference in number of precipitation events between burned and unburned results is small for small thresholds and becomes larger as threshold increases. As intense rainfall rate events (>1 mm day^{-1}) are usually associated with convective storms, we can conclude that burned areas had a stronger impact on convective stronger rainfall events than in non-convective weaker events, thus supporting the hypothesis that burned areas reduces convective instability in the study area. Our regional model results suggest that vegetation and ground condition changes associated with burned areas reduced precipitation in the sub-Sahara

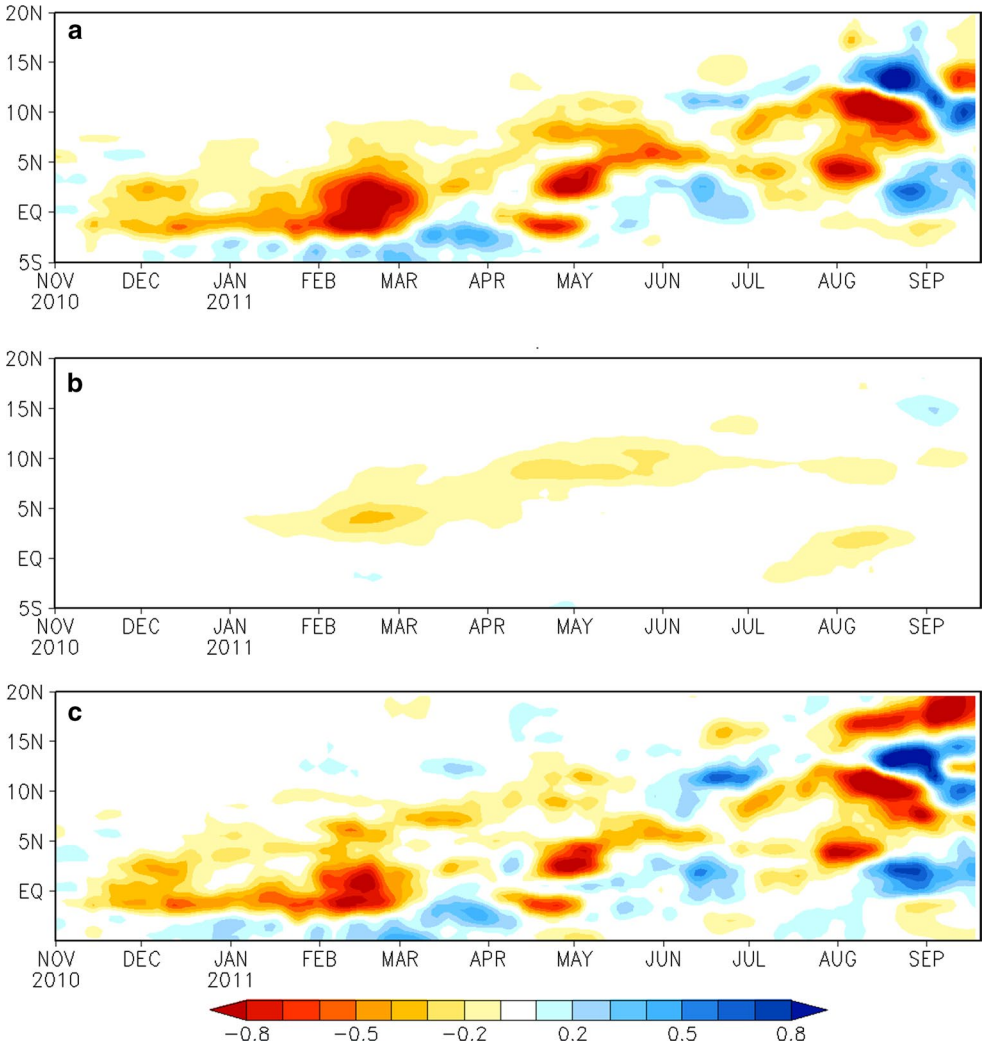

Fig. 14 Time-latitude diagram from Nov 2010 to Sep 2011 of 10-day running mean for **a** precipitation, and **b** surface evapotranspiration, and **c** atmospheric MFC differences between burned and unburned experiments over area A (mm day^{-1})

Table 2 Impact of burned areas on Sahel's monthly and annual mean precipitation for the major land cover types in area A (%)

Land cover	Oct	Nov	Dec	Jan	Feb	Mar	Apr	May	Jun	Jul	Aug	Sep	Year
Rainforests	1.1	−1.4	−4.1	−10.3	−19.2	−5.2	−2.0	−3.2	2.7	−4.4	4.0	2.0	−3.3
Other forests	−0.2	−0.3	−2.0	−6.9	−8.8	−1.1	−0.7	−3.1	−1.0	−0.7	−8.0	1.6	−2.6
Savannas	−0.1	−0.2	−3.8	−6.7	−13.8	−6.9	−4.1	−4.9	−0.2	−2.1	−4.0	0.9	−3.8
Grasslands	0.3	−0.4	−4.0	−5.9	−5.2	−0.5	−1.4	−3.3	1.3	−1.6	−3.1	0.9	−1.9
Shrublands	0.4	−1.3	−1.9	−7.2	−3.6	−0.7	−2.9	−3.1	−0.6	1.0	1.6	−6.6	−2.1
Croplands	0.7	0.3	−2.3	−8.3	−0.4	−1.8	−1.0	−0.5	−0.8	−0.6	0.5	−1.4	−1.3
All land	0.3	−0.8	−3.3	−8.3	−11.6	−3.6	−2.6	−3.8	0.1	−1.4	−2.0	−0.3	−3.2

Shrublands include shrubs with and without ground cover. Only grid points with differences significant at 90 % level of confidence were used in the calculation

Africa, including the Sahel region, by increasing albedo and reducing turbulent heat transfers from land to the atmosphere, which in turn decreased atmospheric upward motion and atmospheric MFC and ultimately weakened convective instability and precipitation in the region.

We also examine the implications of burned-area-induced surface energy and precipitation changes on the region's monthly gross primary productivity (GPP) (Fig. 17). On average, the total amount of carbon fixed by vegetation through photosynthetic assimilation in the area

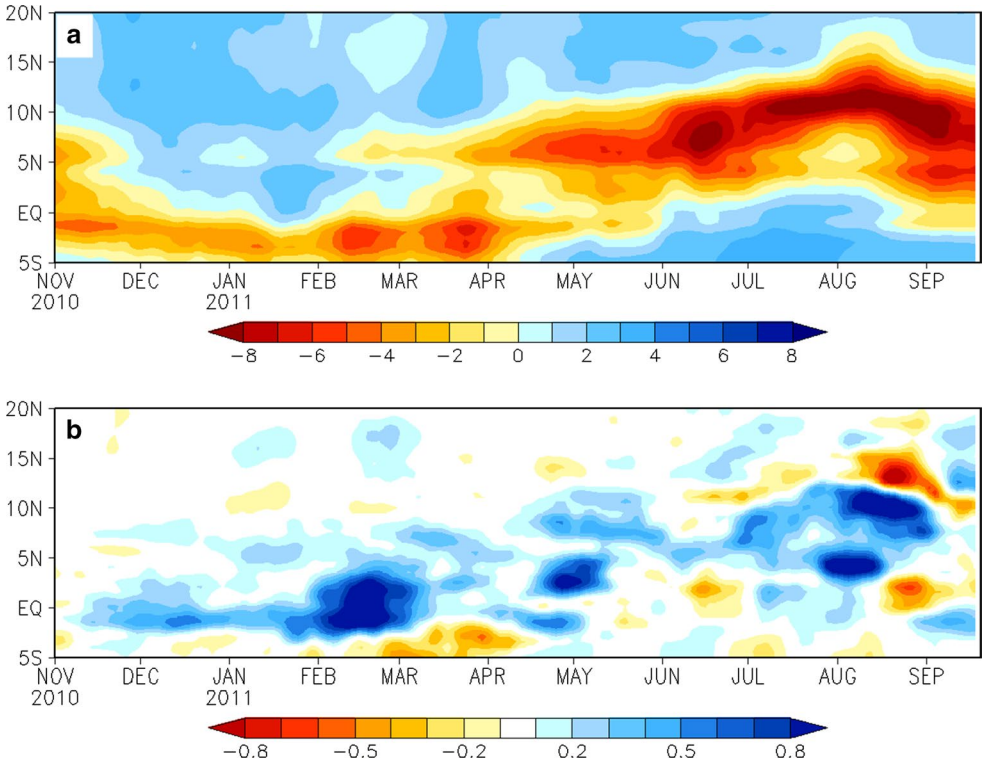

Fig. 15 Time-latitude diagram from Nov 2010 to Sep 2011 of 10-day running mean for **a** 500-hPa vertical velocity and **b** 500-hPa vertical velocity difference between burned and unburned experiments over the area A (10^{-2} Pa s^{-1})

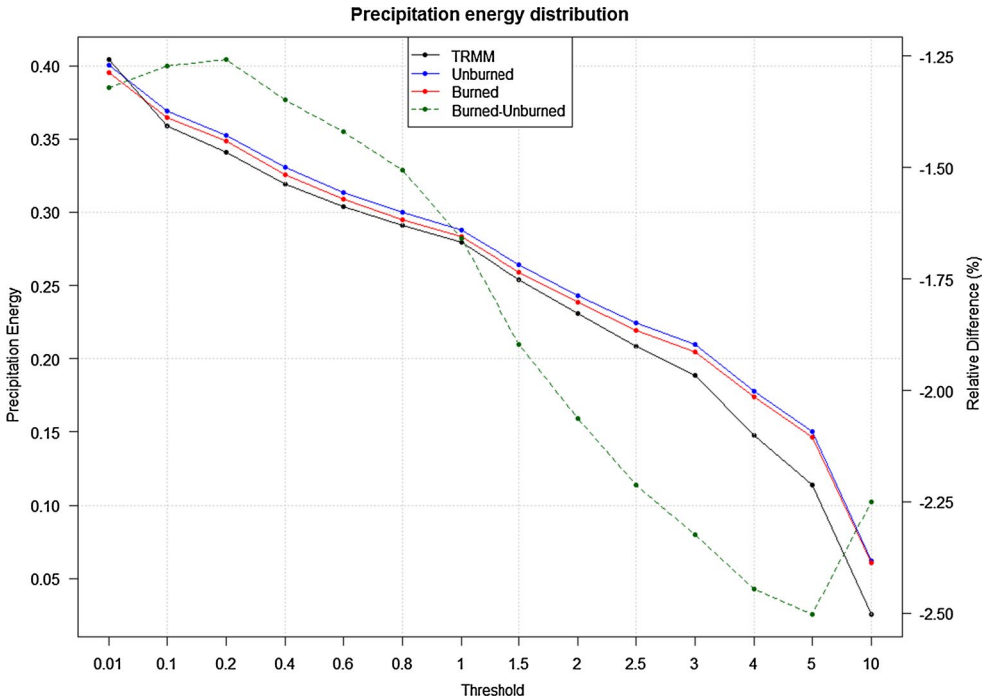

Fig. 16 Daily precipitation energy distributions for TRMM estimates (*black*), unburned (*blue*) and burned (*red*) experiments, and the relative difference between experiments (*green line*)

diminishes every month of simulation. The months with the largest GPP losses are August, July, and June with −248.9, −241.1 and −230.5 gC m^{-2} $year^{-1}$, respectively (Fig. 17a). However, the relative differences (percentage of GPP loss) indicate that period between February and May experienced the strongest impacts with approximately 15 % decrease in GPP. Our results suggest that the decrease in GPP is probably due to a combined effect of vegetation modification during the dry season and precipitation reduction during the wet season.

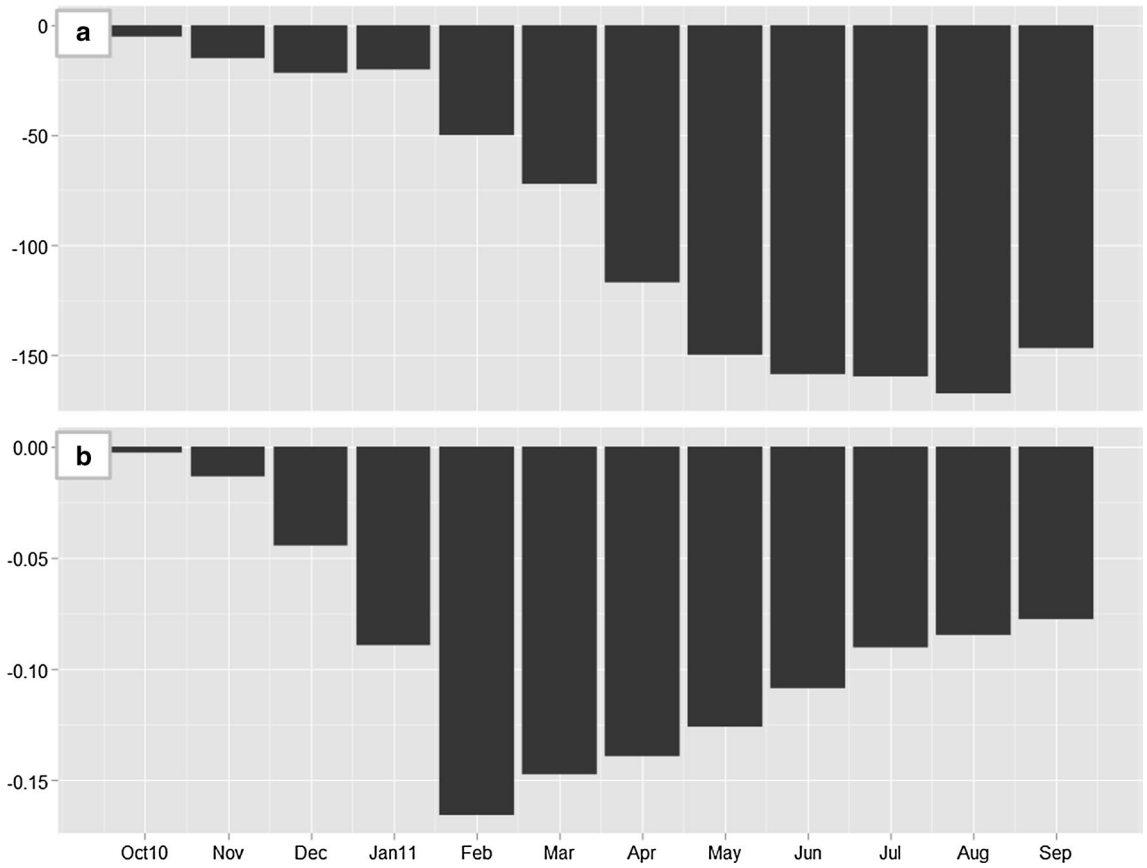

Fig. 17 Monthly mean gross primary product differences (**a**) and relative differences (**b**) between burned and unburned simulations averaged over burned areas within the area A (gC m^{-2} $year^{-1}$ and %)

The modeling results analyzed in this study do not include some important processes that might also affect the response of precipitation and GPP to burned-area-induced circulation and surface energy changes. For example, the role of vegetation regrowth in burned area, which is observed after prolong wet periods is not included in model. This process might have a significant role on the precipitation impact especially during the late phase of the monsoon when new vegetation may contribute to additional evapotranspiration and thus affect surface energy balance and wind circulation.

Similarly, the radiative effect of aerosol particle and carbon emissions during vegetation burning is omitted in the simulations. These emissions can affect the radiation balance leading to further changes in surface energy (Tummon et al. 2010; Wu et al. 2011). In addition, on-going observational study in Southern Africa suggests that charcoal removal period varies for different land cover types and may be longer than the 10-day period utilized in this study for some types. Charcoal removal period is an important variable in modeling studies of burned area impacts on regional climate and requires further investigation.

Furthermore, the temporal averaging approach utilized to generate the burned area information may inadvertently produce larger fractional burned area estimates than actually observed during the October 2010-September 2011 studied period. Consequently, impacts on precipitation and GPP should be interpreted as a first-order approximation.

5 Concluding remarks

This study investigated the impact of burned areas on the monthly and seasonal precipitation in the Northern Africa. Mean burned area fractions were calculated based on MODIS approximate date of burning product, which were then implemented in a set of 1-year-long WRF-NMM/SSiB2 model simulations. In these experiments, vegetation and soil properties were modified based on the burned area fraction and on survival rates for each vegetation land cover type. We also carried out a set of unburned experiments, which did not include any vegetation or soil condition alterations, to provide a benchmark for assessing the impact of burned areas.

Benchmark simulations analysis revealed that the WRF-NMM/SSiB2 was able to simulate the West African monsoon system evolution and intensity. Annual mean precipitation bias and root-mean-squared error over the area of study were approximately 1.1 and 3.0 mm day^{-1}, respectively, based on TRMM estimates. The model also simulated reasonably well the monthly surface air temperature variability patterns over Northern Africa. Annual mean temperature bias and root-mean-squared error averaged over the same area were calculated as 0.1 and 1.4 °C, respectively, based on CAMS observations. Additionally, the analysis of monthly zonal wind pressure-latitude cross-sections revealed that the model can simulate reasonably the key circulation features related to the West African monsoon system evolution, including the upper-level tropical easterly jet, the mid-level African easterly jet, and the low-level tropical westerlies associated with the monsoonal moisture flow from the Atlantic Ocean.

The effects of burned areas in the sub-Saharan Africa's precipitation and surface climate were evident. We found that vegetation condition deterioration due to wildfires increased land surface albedo by exposing the brighter bare ground, which in turn diminished surface net radiation in the burned areas. The drop in surface net radiation resulted initially in a decrease in surface sensible heat flux to atmosphere during winter and early spring, followed by a reduction in evapotranspiration from April onwards through the rainy season. Substantial decrease in atmospheric MFC was also observed in the burned area experiments over the Sahel.

Simulation results indicate that the drying and cooling of atmosphere associated with burned areas led to the strengthening of subsidence during pre-onset and to the weakening of upward motion during onset and mature stages of the monsoon leading to a waning of convective instability and precipitation. Moreover, the precipitation decrease was not limited to the burned regions but included areas with little to no observed wildfires, such as the West African rainforest, indicating that changes in wind circulation and moisture advection outside burned regions also contributed to the total precipitation decrease. Precipitation energy analysis revealed that most of precipitation decrease originated from convective events, which corroborates the hypothesis of convective instability weakening due to burned areas.

Precipitation intensification was observed to the south and north of the main precipitation reduction belt throughout the simulation. From January through May, enhanced precipitation to the south of the Sahel monsoon area formed as favorable conditions for convection arose with the intensification of upward motion and atmospheric MFC there. In summer, intensification of atmospheric MFC and convection also developed to the north and south of the main precipitation reduction belt in the burned area simulations, resulting in increased precipitation in those locations compared to the unburned scenario. Overall, however, precipitation reduction was the more dominant outcome due to the burned-area-induced changes. Results also showed implications of burned area on photosynthetic assimilation. The resulting rainfall decrease and vegetation deterioration caused a drop in GPP in the Sahel. The summer months showed the largest GPP total losses. However, the strongest impacts were observed in late winter and early spring when an approximate 15 % relative decrease in GPP was simulated.

The quantification of the burned-area impacts on precipitation and surface energy and its implications on carbon fluxes between the terrestrial biosphere and the atmosphere are of scientific importance and relevant to our understanding of climate and climate change. This study supports more observational effort and modeling studies on this subject.

Acknowledgments This study was funded by NASA grant NNX-11AQ16G S04 and NSF Grant AGS-1115506. The authors would like to thank Extreme Science and Engineering Discovery Environment (XSEDE) for providing invaluable computer time for the regional model simulations. All the model runs described in this study were carried out at the San Diego Supercomputer Center's computer facility.

References

Bond W, Woodward F, Midgley G (2005) The global distribution of ecosystems in a world without fire. New Phytol 165:525–537

Bowman D, Balch J, Artaxo P, Bond W, Carlson J, Cochrane M, D'Antonio C, DeFries R, Doyle J, Harrison S, Johnston F, Keeley J, Krawchuk M, Kull C, Marston J, Moritz M, Prentice I, Roos C, Scott A, Swetnam T, van der Werf G, Pyne S (2009) Fire in the earth system. Science 324:481–484

Clark D, Xue Y, Harding R, Valdes P (2001) Modeling the impact of land surface degradation on the climate of tropical north Africa. J Clim 14:1809–1822

Courel M, Kandel R, Rasool S (1984) Surface albedo and the Sahel drough. Nature 307:528–531

De Sales F, Xue Y (2011) Assessing the dynamic-downscaling ability over South America using the intensity-scale verification technique. Int J Climatol 31:1205–1221

De Sales F, Xue Y (2013) Dynamic downscaling of 22-year CFS winter seasonal hindcasts with the UCLA-ETA regional climate model over the United States. Clim Dyn 41:255–275

Fan Y, van den Dool H (2008) A global monthly land surface air temperature analysis for 1948-present. J Geophys Res. doi:10.1029/2007JD008470

Ferrier B (1994) A double-moment multiple-phase 4-class buld ice scheme. 1 description. J Atmos Sci 51:249–280

Giannini A, Saravanan R, Chang P (2003) Oceanic forcing of Sahel rainfall on interannual to interdecadal time scales. Science 302:1027–1030

Glenn-Lewin DC, van der Maarel E (1992) Patterns and processes of vegetation dynamics. In: Glenn-Lewin DC, Peet RK, Veblen TT (eds) Plant succession: theory and prediction. Chapman and Hall, London, pp 11–59

Govaerts Y, Pereira J, Pinty B, Mota B (2002) Impact of fires on surface albedo dynamics over the African continent. J Geophys Res-Atmos 107(D22), 4629. doi:10.1029/2002JD002388

Huffman GJ, Adler RF, Bolvin DT, Gu G, Nelkin EJ, Bowman KP, Hong Y, Stocker EF, Wolff DB (2007) The TRMM multi-satellite precipitation analysis: quasi-global, multi-year, combined-sensor precipitation estimates at fine scale. J Hydrometeorol 8(1):38–55

Janjic ZI (1994) The step-mountain eta coordinate model: further developments of the convection, viscous sublayer, and turbulence closure schemes. Mon Weather Rev 122:927–945

Janjic Z (2003) A nonhydrostatic model based on a new approach. Meteorol Atmos Phys 82:271–285

Janjic Z, Gerrity J, Nickovic S (2001) An alternative approach to non-hydrostatic modeling. Mon Weather Rev 129:1164–1178

Jin Y, Roy D (2005) Fire-induced albedo change and its radiative forcing at the surface in northern Australia. Geophys Res Lett 32:L13401. doi:10.1029/2005GL022822

Kanamitsu M, Ebisuzaki W, Woollen J, Yang S, Hnilo J, Fiorino M, Potter G (2002) NCEP-DOE AMIP-II reanalysis (R-2). Bull Am Meteorol Soc 83:1631–1643

Lacis AA, Hansen JE (1974) Parameterization for absorption of solar-radiation in Earth's atmosphere. J Atmos Sci 31:118–133

Li K, Coe M, Ramankutty N, De Jong R (2007) Modeling the hydrological impact of land-use change in West Africa. J Hydrol 337:258–268

Los SO, Collatz GJ, Sellers PJ, Malmstrom CM, Pollack NH, DeFries RS, Bounoua L, Parris MT, Tucker CJ, Dazlich DA (2000) A global 9-year biophysical land surface dataset from NOAA AVHRR data. J Hydrometeorol 1:183–199

Lyons E, Jin Y, Randerson J (2008) Changes in surface albedo after fire in boreal forest ecosystems of interior Alaska assessed using MODIS satellite observations. J Geophys Res 113:G02012. doi:10.1029/2007JG000606

Ma H, Mechoso C, Xue Y, Xiao H, Neelin J, Ji X (2013) On the connection between continental-scale land surface processes and the tropical climate in a coupled ocean-atmosphere-land system. J Clim 26:9006–9025

Myhre G, Govaerts Y, Haywood J, Berntsen T, Lattanzio A (2005) Radiative effect of surface albedo change from biomass burning. Geophys Res Lett 32:L20812. doi:10.1029/2005GL022897

Roy D, Lewis P, Justice C (2002) Burned area mapping using multi-temporal moderate spatial resolution data: a bi-directional reflectance model-based expectation approach. Remote Sens Environ 83:263–286

Roy D, Boschetti L, Justice C, Ju J (2008) The collection 5 MODIS burned area product: global evaluation by comparison with the MODIS active fire product. Remote Sens Environ 112:3690–3707

Samain O, Kergoat L, Hiernaux P, Guichard F, Mougin E, Timouk F, Lavenu F (2008) Analysis of the in situ and MODIS albedo variability at multiple timescales in the Sahel. J Geophys Res 113:D14119. doi:10.1029/2007JD009174

Scholes R, Ward D, Justice C (1996) Emissions of trace gases and aerosol particles due to vegetation burning in southern hemisphere Africa. J Geophys Res Atmos 101:23677–23682

Schwarzkopf MD, Fels SB (1991) The simplified exchange method revisited: an accurate, rapid method for computation of infrared cooling rates and fluxes. J Geophys Res Atmos 96:9075–9096

Sultan B, Janicot S (2003) The West African monsoon dynamics. Part II: the "preonset" and "onset" of the summer monsoon. J Clim 16:3407–3427

Thonicke K, Venevsky S, Sitch S, Cramer W (2001) The role of fire disturbance for global vegetation dynamics: coupling fire into a dynamic global vegetation model. Glob Ecol Biogeogr 10:661–677

Tummon F, Solmon F, Liousse C, Tadross M (2010) Simulation of the direct and semidirect aerosol effects on the southern Africa regional climate during the biomass burning season. J Geophys Res 115:D19206. doi:10.1029/2009JD013738

van der Werf G, Randerson J, Giglio L, Collatz G, Mu M, Kasibhatla P, Morton D, DeFries R, Jin Y, van Leeuwen T (2010) Global fire emissions and the contribution of deforestation, savanna, forest, agricultural, and peat fires (1997–2009). Atmos Chem Phys 10:11707–11735

Wu L, Su H, Jiang JH (2011) Regional simulation of deep convection and biomass burning over South America: biomass burning aerosol effects on clouds and precipitation. J Geophys Res 116:D17209. doi:10.1029/2011JD016106

Xue Y (1997) Biosphere feedback on regional climate in tropical north Africa. Q J R Meteorol Soc 123:1483–1515

Xue Y, Shukla J (1993) The influence of land-surface properties on Sahel climate. 1 Desertification. J Clim 6:2232–2245

Xue Y, Liou K, Kasahara A (1990) Investigation of biophysical feedback on the African climate using a 2-dimentional model. J Clim 3:337–352

Xue Y, Sellers PJ, Kinter JL, Shukla J (1991) A simplified biosphere model for global climate studies. J Clim 4:345–364

Xue Y, De Sales F, Vasic R, Mechooso CR, Prince SD, Arakawa A (2010a) Global and temporal characteristics of seasonal climate/vegetation biophysical process (VBP) interactions. J Clim 23:1411–1433

Xue Y, De Sales F, Lau WKM, Boone A, Feng J, Dirmeyer P, Guo Z, Kim K-M, Kitoh A, Kumar V, Poccard-Leclercq I, Mahowald N, Moufouma-Okia W, Pegion P, Rowell DP, Schemm J, Schubert SD, Sealy A, Thiaw WM, Vintzileos A, Williams SF, Wu M-LC (2010b) Intercomparison and analyses of the climatology of the west African monsoon in the west African monsoon modeling and evaluation project (WAMME) first model intercomparison experiment. Clim Dyn 35:3–27

Xue Y, Janjic Z, Dudhia J, Vasic R, De Sales F (2014) A review on regional dynamical downscaling in intraseasonal to seasonal simulation/prediction and major factors that affect downscaling ability. Atmos Res 147–148:68–85

Zeng N, Neelin J, Lau K, Tucker C (1999) Enhancement of interdecadal climate variability in the Sahel by vegetation interaction. Science 286:1537–1540

Zhan XW, Xue YK, Collatz GJ (2003) An analytical approach for estimating CO_2 and heat fluxes over the Amazonian region. Ecol Model 162:97–117

Zheng X, Eltahir E (1997) The response to deforestation and desertification in a model of West African monsoons. Geophys Res Lett 24:155–158